

# Self-Supervised Learning for Real-World Super-Resolution from Dual Zoomed Observations

Zhilu Zhang<sup>1</sup>, Ruohao Wang<sup>1</sup>, Hongzhi Zhang<sup>1</sup>, Yunjin Chen, Wangmeng Zuo<sup>1</sup>

<sup>1</sup>Harbin Institute of Technology, China

{cszllzhang, rhwangHIT}@outlook.com zhanghz0451@gmail.com

chenyunjin\_nudt@hotmail.com wmzuo@hit.edu.cn

## Abstract

In this paper, we consider two challenging issues in reference-based super-resolution (RefSR), (i) how to choose a proper reference image, and (ii) how to learn real-world RefSR in a self-supervised manner. Particularly, we present a novel self-supervised learning approach for real-world image SR from observations at dual camera zooms (SelfDZSR). For the first issue, the more zoomed (telephoto) image can be naturally leveraged as the reference to guide the SR of the lesser zoomed (short-focus) image. For the second issue, SelfDZSR learns a deep network to obtain the SR result of short-focus image and with the same resolution as the telephoto image. For this purpose, we take the telephoto image instead of an additional high-resolution image as the supervision information and select a patch from it as the reference to super-resolve the corresponding short-focus image patch. To mitigate the effect of various misalignment between the short-focus low-resolution (LR) image and telephoto ground-truth (GT) image, we design a degradation model and map the GT to a pseudo-LR image aligned with LR. Then the pseudo-LR and LR image can be fed into the proposed adaptive spatial transformer networks (AdaSTN) to deform the LR features. During testing, SelfDZSR can be directly deployed to super-solve the whole short-focus image with the reference of telephoto image. Experiments show that our method achieves better quantitative and qualitative performance against state-of-the-arts. The code and pre-trained models will be publicly available.

## 1. Introduction

Image super-resolution (SR) aiming to recover a high-resolution (HR) image from its low-resolution (LR) counterpart is a severely ill-posed inverse problem with many practical applications. To relax the ill-posedness of the SR, reference-based image SR (RefSR) has recently been suggested to super-resolve the LR image with more accurate details by leveraging a reference (Ref) image containing similar content and texture with the HR image. Albeit

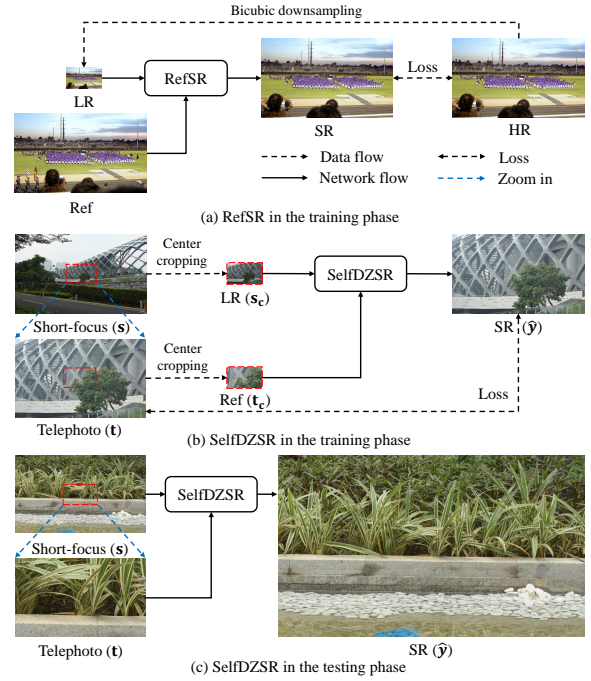


Figure 1. Overall pipeline of RefSR methods and SelfDZSR.

progress has been made in RefSR, it remains a challenging issue to choose a proper reference image for each LR image.

Fortunately, advances and popularity of imaging techniques make it practically feasible to collect images of a scene at two different camera zooms (*i.e.*, dual zoomed observations). For example, asymmetric cameras with multiple fixed-focal lenses have been equipped in modern smartphones. In these practical scenarios, the more zoomed (telephoto) image can be naturally leveraged as the reference to guide the SR of the lesser zoomed (short-focus) image. Image SR from dual zoomed observations (DZSR) can thus be regarded as a special case of RefSR, in which Ref has the same scene as the middle part of the LR image but is with higher resolution. While conventional RefSR methods [21, 30, 35, 48, 49, 56] usually use synthetic (*e.g.*, bicubic) degraded LR images for training and evaluation (see



Figure 2. Misalignment between LR (left) and GT (right) after flow-based alignment. The lines with the same color are on the same horizontal line, but the length is different.

Fig. 1(a)), DZSR should cope with real-world LR short-focus images and no ground-truth HR images are available in training. To bridge the domain gap between synthetic and real-world LR images, dual-camera super-resolution (DCSR) [40] suggests self-supervised real-image adaptation (SRA) involving a degradation preserving and a detail transfer terms. However, DCSR only attains limited success, due to that the two loss terms in SRA cannot well address the gap between the synthetic and real-world LR degradation as well as the misalignment between short-focal and telephoto images.

In this work, we aim at super-resolving the real world short-focal image with the reference of the corresponding telephoto image. Different from DCSR [40] requiring to pre-train on synthetic images, we adopt self-supervised learning to train DZSR model (*i.e.*, SelfDZSR) from scratch directly on paired short-focal and telephoto images. As shown in Fig. 1(b), instead of the whole images, during training we crop the center part of the short-focus and telephoto image respectively as the input LR and Ref, and use the whole telephoto image as the ground-truth (GT). In the testing phase, by using the whole short-focus and telephoto images respectively as LR and Ref, SelfDZSR can be directly deployed to super-solve the whole short-focus image (See Fig. 1(c)).

However, when training SelfDZSR, the cropped short-focus image generally cannot be accurately aligned with the telephoto GT image, making the learned model prone to producing blurry SR results [55]. From Fig. 2, the misalignment can be very complex. Off-the-shelf optical flow estimation (*e.g.*, PWC-Net [37]) is limited in offset diversity [5], and works poor in SelfDZSR. Inspired by [5, 7, 55], we propose adaptive spatial transformer networks (AdaSTN) for better handling the misalignment issue. Particularly, we first train a degradation model for mapping the GT to a pseudo-LR image that is ideally aligned with GT. Then the pseudo-LR and the original LR images are fed into a pixel-level AdaSTN for estimating the offsets between them to deform the LR features. AdaSTN implicitly aligns contents between LR and pseudo-LR by minimizing the reconstruction loss. When training is done, the offset estimator of AdaSTN and degradation model can be safely detached. That is, the estimated offsets of AdaSTN can be set by default, bringing no extra cost in the test phase.

Moreover, for better exploiting Ref, another key issue in SelfDZSR is to search corresponding contents from Ref for LR image. Most existing RefSR methods [21, 30, 40, 49, 56] perform similarity matching between LR and Ref features. But for SelfDZSR, the LR and GT are not inaccurately aligned, and matching Ref to LR may bring more uncertainty. Thus, we instead calculate the correlation between the pseudo-LR and Ref features. Then we feed the pseudo-LR and warped Ref features into AdaSTN for finer alignment. In the testing phase, the pseudo-LR image can be replaced by the LR image. By this way, we can ensure that the deformed Ref features are approximately aligned with GT during training, and aligned with LR during testing. Finally, the deformed LR and deformed Ref features can be regarded as aligned with GT, which are then combined and fed into the restoration module.

Extensive experiments are conducted on the Nikon camera from the DRealSR dataset [44] as well as the CameraFusion dataset [40]. The results demonstrate the effectiveness and practicability of our SelfDZSR for real-world image SR from dual zoomed observations. In comparison to the state-of-the-art SR and RefSR methods, our SelfDZSR performs favorably in terms of both quantitative metrics and perceptual quality.

To sum up, the main contributions of this work include:

- An effective self-supervised learning approach, *i.e.*, SelfDZSR, is presented to super-resolve the real-world images from dual zoomed observations.
- Adaptive spatial transformer networks (AdaSTN) are suggested to alleviate the adverse effect of image misalignment between LR and GT, while bringing no extra inference cost.
- Quantitative and qualitative results on Nikon camera and CameraFusion show that our method outperforms the state-of-the-art methods.

## 2. Related Work

### 2.1. Blind Image Super-Resolution

With the development of deep networks, single image super-resolution (SISR) methods based on fixed and known degradation have achieved great success in terms of both performance [11, 25, 28, 51, 54] and efficiency [18, 24, 29, 38, 47]. However, these methods perform poorly when applying to images with an unknown degradation, and may cause some artifacts. Thus, blind super-resolution comes into being to bridge the gap.

On the one hand, some works estimate the blur kernel or degradation representation for LR and feed it into the SR reconstruction network. IKC [15] performed kernel estimation and SR reconstruction processes iteratively, while DAN [33] conducted it in an alternating optimization scheme. KernelGAN [1] utilized the image patch recurrence property to estimate an image-specific kernel, and

FKP [27] learned a kernel prior based on normalization flow [10] at test time. To relaxing the assumption that blur kernels are spatially invariant, MANet [26] estimated spatially variant kernel by suggesting mutual affine convolution. Different from the above explicit methods of estimating kernel, DASR [39] introduced contrastive learning [16] to extract discriminative representations to distinguish different degradations. On the other hand, Hussein *et al.* [19] modified the LR to a pre-defined degradation (*e.g.*, bicubic) type by a closed-form correction filter. BSRGAN [50] and Real-ESRGAN [41] designed more complex degradation models to generate LR data for training the networks, making the networks generalize well to many real-world degradation scenarios.

## 2.2. Real-World Image Super-Resolution

Although blind SR models trained on synthetic data have shown appreciable generalization capacity, the formulated degradation assumption limits the performance on real-world images with much more complicated and changeable degradation. Thus, image SR directly towards real-world scenes has also received much attention. On the one hand, given unpaired real LR and HR, several real-world SR methods [3, 43, 45] attempt to approximate real degradation and generate the pseudo-LR image from HR, and then learn to super-resolve the pseudo-LR in a supervised manner. On the other hand, some methods [4, 6, 31, 32, 44] construct paired datasets by adjusting the focal length of a camera, in which the image with a long focal and short focal length is regarded as GT and LR, respectively. Among these methods, LP-KPN [4] presented a kernel prediction network based on the Laplacian pyramid. CDC [44] considered reconstruction difficulty of different components, performed real-world image SR in a divide-and-conquer manner.

In addition, the misalignment of data pairs is a universal problem in real scenes, and it may cause blurry SR result. The above methods based on paired datasets pre-execute complex alignment or even manual selection, which are generally laborious and time-consuming. Different from them, CoBi [53] loss offered an effective way to deal with misalignment during SR training. Zhang *et al.* [55] incorporated global color mapping and optical flow [37] to explicitly align the data pairs with severe color inconsistency. Nevertheless, optical flow is limited in handling complicated misalignment (see Fig. 2). In this work, we further propose AdaSTN to handle the complicated misalignment after pre-alignment with optical flow.

## 2.3. Reference-Based Image Super-Resolution

RefSR aims to take advantage of a high-resolution reference image that has similar content and texture as LR for super-resolution. It relaxes the ill-posedness of SISR and facilitates the generation of more accurate details. The features extracting and matching between LR and Ref is

the research focus of most RefSR methods. Among them, Zheng *et al.* [57] proposed a correspondence network to extract features for matching, and an HR synthesis network with the input of the matched Ref. SRNTT [56] calculated the correlation between pre-trained VGG features of LR and Ref at multiple levels for matching them. Furthermore, TTSR [49] and FRM [48] developed an end-to-end training framework and proposed learnable feature extractors. Recently,  $C^2$ -Matching [21] performed a more accurate match by the teacher-student correlation distillation while MASA-SR [30] reduced the computational cost by coarse-to-fine correspondence matching. Besides, CrossNet [58] and SEN [35] respectively introduced optical flow [12] and deformable convolution [7, 59] to align Ref with LR. However, optical flow is limited in handling large and complicated motions while deformable convolution is limited in modeling long-distance correspondence. In this work, we follow [21] to perform patch-wise matching.

Additionally, the RefSR methods mentioned above are all based on the bicubic down-sampling. DCSR [40] explores an adaptive fine-tuning strategy on real-world images based on the pre-trained model with synthetic data. In this work, we propose a fully self-supervised learning framework directly on weakly aligned dual zoomed observations.

## 3. Proposed Method

In this section, we first give a description of our self-supervised learning framework for super-resolution from dual zoomed observations. Then we detail the solutions for handling the misalignment problem, not only between LR and GT, but also between Ref and GT. Next, the design of the restoration module is introduced, and the learning objectives are further provided.

### 3.1. Self-Supervised Learning Framework

Denote by  $s$  and  $t$  the short-focus image and the telephoto image, respectively. Super-resolution based on dual zoomed observations aims to super-resolve the short-focus image  $s$  with the reference telephoto image  $t$ , which can be written as,

$$\hat{y} = \mathcal{Z}(s, t; \Theta_{\mathcal{Z}}), \quad (1)$$

where  $\hat{y}$  has the same field-of-view as  $s$  and the same resolution as  $t$ ,  $\mathcal{Z}$  denotes the zooming network with the parameter  $\Theta_{\mathcal{Z}}$ .

However, in real-world scenarios, the GT of  $\hat{y}$  is hard or almost impossible to acquire. A simple alternative solution is to leverage synthetic data for training, but the domain gaps between the degradation model in training and that in real-world images prevent it from working well. DCSR [40] tries to bridge the gaps by fine-tuning the trained model using an SRA strategy, but the huge difference in the field of view between the output and the target telephoto image limits it in achieving satisfying results.

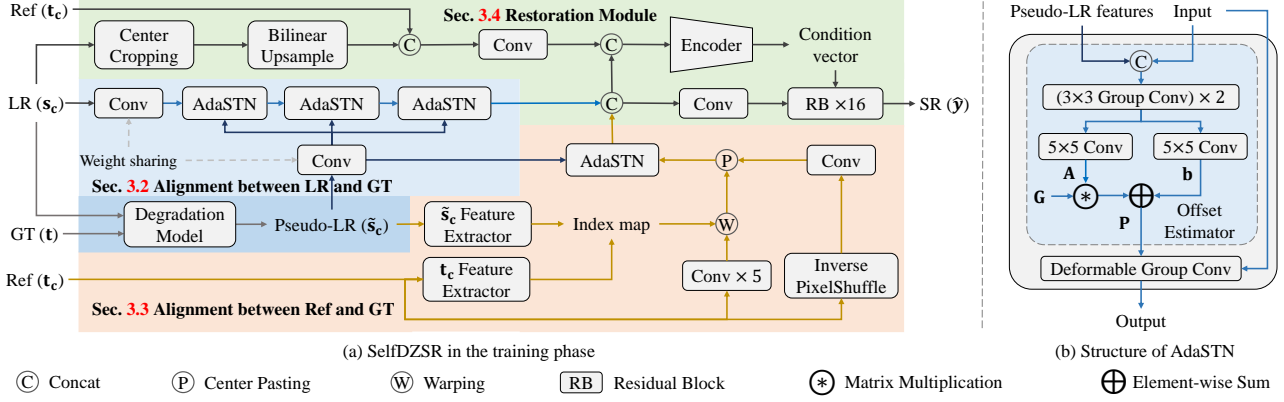


Figure 3. The detailed pipeline of proposed SelfDZSR. (a) SelfDZSR in the training phase. Pseudo-LR is generated from the degradation model for alignment between LR and GT. The aligned LR and Ref features are fed into the restoration module. Each color block corresponds to a subsection. (b) Structure of AdaSTN.

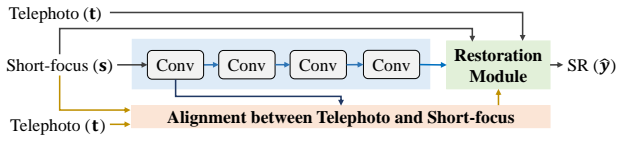


Figure 4. SelfDZSR during testing. The short-focus and telephoto image can be regarded as LR and Ref, respectively. The degradation model is detached and AdaSTN is simplified to a convolution layer. The colors of the blocks and lines correspond to Fig. 3(a).

In contrast to the above methods, we propose a novel self-supervised dual-zooms super-resolution (SelfDZSR) framework, which can be trained from scratch solely on paired short-focal and telephoto image (see Fig. 1(b)), and be directly deployed to the real-world dual zoomed observations (see Fig. 1(c)). During training, we first crop the central area of the telephoto and short-focus images that have the same size,

$$s_c = \mathcal{C}(s; r), \quad t_c = \mathcal{C}(t; r), \quad (2)$$

where  $\mathcal{C}$  denotes the center cropping operator,  $r$  is the focal length ratio of  $t$  and  $s$ . Note that  $t_c$  has the same scene with  $\mathcal{C}(s_c; r)$ , i.e., the central area of  $s_c$ , and has the same size as  $s_c$ . Moreover,  $t$  and  $s_c$  have the same scene, but the resolution is different by  $r$  times. Thus,  $s_c$  and  $t_c$  can be naturally used as LR and Ref respectively, while  $t$  can be regarded as the GT. Then we can define SelfDZSR as,

$$\Theta_Z = \arg \min_{\Theta_Z} \mathcal{L}(\mathcal{Z}(s_c, t_c; \Theta_Z), t) \quad (3)$$

where  $\mathcal{L}$  denotes the self-supervised learning objective. Nonetheless, both  $t_c$  and  $t$  are not spatially aligned with  $s_c$ , and elaborate design on network architecture and loss terms is thus essential for SelfDZSR.

### 3.2. Alignment between LR and GT

Obviously, the LR image  $s_c$  and GT image  $t$  are captured from the different camera lens, and thus are misaligned in space. Recent study [55] has shown that the misalignment of data pairs will cause the network to produce blurry and even pixel-shifted results. Optical flow [37] offers a probable solution in dealing with this issue. However, limited

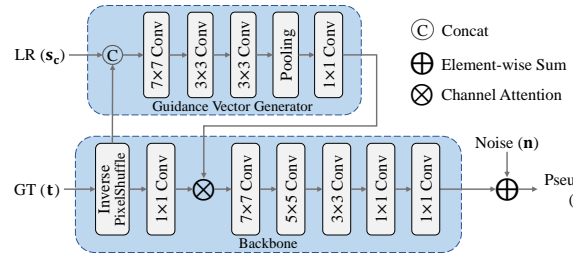


Figure 5. Illustration of the deep degradation model.

to the offset diversity [5] of optical flow, images after registration are still slightly misaligned in some complex circumstances and explicit alignment is very difficult. Instead, we suggest to implicitly align LR to GT during training the deep restoration model.

The LR image  $s_c$  can be treated as a degraded and spatially deformed observation of GT  $t$ . In order to align LR to GT, both the degradation and misalignment should be taken into account. Therefore, our alignment scheme also involves two modules. That is, we first map GT to a pseudo-LR that has similar degradation types with LR, and then estimate the offsets between pseudo-LR and LR.

**Mapping GT  $t$  to pseudo-LR  $\tilde{s}_c$ .** We first design a degradation network for blurring and down-sampling the GT, and then add random noise to it. Thus, the degradation model can be written as,

$$\tilde{s}_c = \mathcal{D}(t, s_c; \Theta_D) + n, \quad (4)$$

where  $\mathcal{D}$  denotes the degradation network with the parameter  $\Theta_D$ ,  $n$  denotes the noise detailed in the suppl. Fig. 5 illustrates the deep degradation model. In particular, LR  $s_c$  is used to generate a conditional guidance vector for modulating features of  $t$  globally. Simultaneously, the spatial position of pseudo-LR should keep the same as GT. In order to achieve this, we take advantage of the centroid loss to constrain the weight of the convolution kernel in the backbone, which will be described in Sec. 3.5.

**Aligning LR  $s_c$  to pseudo-LR  $\tilde{s}_c$ .** Given LR and pseudo-LR (aligned with GT), we can estimate the offsets between them and then deform the LR features (see



Fig. 3(a)). Deformable convolution [7] is a natural choice, but it may cause the training process to be unstable when estimating the offsets directly. Inspired by [13], we propose pixel-level adaptive spatial transformer networks (AdaSTN) as shown in Fig. 3(b). For every pixel, the estimated offset of AdaSTN can be written as,

$$\mathbf{P} = \mathbf{A}\mathbf{G} + \mathbf{b}, \quad (5)$$

where  $\mathbf{A} \in \mathbb{R}^{2 \times 2}$  is a predicted affine transformation matrix and  $\mathbf{b} \in \mathbb{R}^{2 \times 1}$  is the translation vector.  $\mathbf{G}$  is a regular grid represented by

$$\mathbf{G} = \begin{bmatrix} -1 & -1 & -1 & 0 & 0 & 0 & 1 & 1 & 1 \\ -1 & 0 & 1 & -1 & 0 & 1 & -1 & 0 & 1 \end{bmatrix}. \quad (6)$$

Thus, the deformable convolution of AdaSTN can be formulated as,

$$\mathbf{y}(\mathbf{q}) = \sum_{k=0}^8 \mathbf{w}_k \mathbf{x}(\mathbf{q} + \mathbf{p}_k), \quad (7)$$

where  $\mathbf{x}$  and  $\mathbf{y}$  represent the input and output features, respectively.  $\mathbf{w}_k$  denotes the kernel weight and  $\mathbf{p}_k$  denotes the  $k$ -th column value of  $\mathbf{P}$ . AdaSTN can be regarded as a variant of STN [20], which is from a global mode to a pixel-wise mode. In comparison to deformable convolution [7], AdaSTN is more stable in estimating the offsets. During experiments, we stack three AdaSTNs to align LR and pseudo-LR progressively.

Note that pseudo-LR is not available in the testing phase. A feasible way is to replace pseudo-LR with LR. Actually, there is no need to estimate the offsets for AdaSTN. We can set  $\mathbf{P} = \mathbf{0}$  directly, which means that the deformable convolution of AdaSTN can only observe the input value at the center point of the kernel and degenerates into  $1 \times 1$  convolution (see Fig. 4). However, this way may produce some artifacts in results due to the gap between training and testing. In order to bridge this gap, for each AdaSTN, we randomly set  $\mathbf{P} = \mathbf{0}$  for the samples in a batch with probability  $p$  (e.g., 0.3) during training. For each training sample, the probability  $p^3$  (e.g., 0.027) that three AdaSTNs are all set to  $\mathbf{P} = \mathbf{0}$  is low, so it has little impact on the learning of the overall framework.

### 3.3. Alignment between Ref and GT

Matching between Ref and LR is an important issue in RefSR. Previous methods generally perform matching by calculating feature similarity. When LR is not aligned with GT, aligning Ref to LR may bring more uncertainty. Thus, we instead calculate the correlation between the features of Ref and pseudo-LR (aligned with GT) for matching (see Fig. 3(a)). The feature extractor is pretrained by knowledge distillation proposed by  $C^2$ -Matching [21].

In addition, for SelfDZSR, the central part of LR have the same scene with Ref. Taking this property into account, we can paste the Ref features after Inverse PixelShuffle layer to the center area of the warped Ref. Then an AdaSTN is used for finer alignment. During testing, the pseudo-LR features can be substituted by LR features (see Fig. 4).

### 3.4. Restoration Module

After getting the aligned LR and aligned Ref features, we concatenate and feed them into the backbone of the restoration module consisting of 16 residual blocks [28]. The concatenated features are also fed into an encoder to generate condition vectors for global modulation of the backbone features. The role of modulation is to make better use of Ref information and relieve the color inconsistency between short-focus and telephoto images. For better global modulation, we also combine the original Ref features with the central area features of LR to enrich the input features of the encoder, as shown in Fig. 3(a). Note that the output of the encoder is the vector, so the weak misalignment between LR and the central area of Ref affects little on the global modulation. The details of encoder and modulation will be introduced in the suppl.

### 3.5. Learning Objective

The degradation network and SelfDZSR are optimized separately. In the following, we introduce the loss terms for degradation network and SelfDZSR, respectively.

**Loss terms for degradation network.** The degradation network is trained with a combination of  $\ell_1$  loss and centroid loss, which can be written as,

$$\mathcal{L}_D(\tilde{\mathbf{s}}_c, \mathbf{s}_c, \mathbf{n}) = \|(\tilde{\mathbf{s}}_c - \mathbf{n}) - \mathbf{s}_c\|_1 + \lambda_c \sum_{l=1}^L \mathcal{L}_c(\mathbf{W}^l), \quad (8)$$

where  $\lambda_c = 100$ ,  $\mathbf{W}^l$  denotes the kernel weight parameters of the  $l$ -th convolution layer in the backbone of the degradation network. The centroid loss  $\mathcal{L}_c$  can be defined as,

$$\begin{aligned} \mathcal{L}_c(\mathbf{W}^l) = & \left\| \sum_{i=0}^{k-1} \sum_{j=0}^{k-1} \left( i - \frac{k}{2} + 0.5 \right) w_{i,j}^l \right\|_1 \\ & + \left\| \sum_{i=0}^{k-1} \sum_{j=0}^{k-1} \left( j - \frac{k}{2} + 0.5 \right) w_{i,j}^l \right\|_1, \end{aligned} \quad (9)$$

where  $k$  is odd and denotes the kernel size,  $w_{i,j}^l$  denotes the value in the  $(i, j)$  position of  $\mathbf{W}^l$ . The centroid loss is introduced to constrain that the centroid of the convolution kernel is in the center of space, thereby ensuring that the pseudo-LR is aligned with GT.

**Loss terms for SelfDZSR.** The sliced Wasserstein (SW) distance has exhibited outstanding merit for training deep generative networks [9, 46]. Recently, SW loss has been successfully applied in texture synthesis [17], image enhancement [8] and *etc.* Here, we also use SW loss  $\mathcal{L}_{SW}$  to optimize SelfDZSR, the detailed description will be given in the suppl. The loss term of SelfDZSR can be written as,

$$\mathcal{L}_{\text{SelfDZSR}}(\hat{\mathbf{y}}, \mathbf{t}) = \|\hat{\mathbf{y}} - \mathbf{t}\|_1 + \lambda_{SW} \mathcal{L}_{SW}(\phi(\hat{\mathbf{y}}), \phi(\mathbf{t})), \quad (10)$$

where  $\phi$  denotes the pre-trained VGG-19 [36] network, and we set  $\lambda_{SW} = 0.08$ .

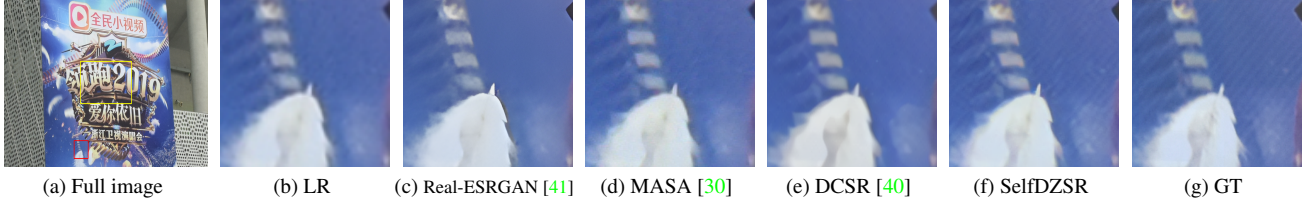


Figure 6. Visual comparison on Nikon camera images. Due to the limitation of space, here we select three methods with better LPIPS [52] (related to perceptual quality) for comparison. In the full image, the yellow box indicates the overlapped scene between LR and Ref, while the red box represents the selected LR patch. Our result in sub-figure (f) restores much more details (diagonal white stripes).

Table 1. Quantitative results on Nikon camera images. We mark the best results in **bold**. The models trained only with  $\ell_1$  (or  $\ell_2$ ) loss are marked in gray. RefSR<sup>†</sup> represents that the RefSR methods are trained in our self-supervised learning manner.

|                    | Method                         | # Param<br>(M) | <i>Full-Image</i>                                      |  | <i>Corner-Image</i>                                    |  |
|--------------------|--------------------------------|----------------|--|--|--|--|
|                    |                                |                | PSNR $\uparrow$ / SSIM $\uparrow$ / LPIPS $\downarrow$ |  | PSNR $\uparrow$ / SSIM $\uparrow$ / LPIPS $\downarrow$ |  |
| SISR               | EDSR [28]                      | 43.1           | 27.26 / 0.8364 / 0.362                                 |  | 27.29 / 0.8345 / 0.363                                 |  |
|                    | RCAN [54]                      | 15.6           | 27.30 / 0.8344 / 0.383                                 |  | 27.33 / 0.8323 / 0.383                                 |  |
|                    | CDC [44]                       | 39.9           | 27.20 / 0.8306 / 0.412                                 |  | 27.24 / 0.8283 / 0.412                                 |  |
|                    | BSRGAN [50]                    | 16.7           | 26.91 / 0.8151 / 0.279                                 |  | 26.96 / 0.8135 / 0.278                                 |  |
|                    | Real-ESRGAN [41]               | 16.7           | 25.96 / 0.8076 / 0.272                                 |  | 26.00 / 0.8063 / 0.271                                 |  |
| RefSR <sup>†</sup> | SRNTT- $\ell_2$ [56]           | 5.5            | 27.30 / 0.8387 / 0.359                                 |  | 27.33 / 0.8366 / 0.359                                 |  |
|                    | SRNTT [56]                     | 5.5            | 27.31 / 0.8242 / 0.286                                 |  | 27.35 / 0.8223 / 0.283                                 |  |
|                    | TTSR- $\ell_1$ [49]            | 7.3            | 25.83 / 0.8272 / 0.369                                 |  | 25.80 / 0.8259 / 0.369                                 |  |
|                    | TTSR [49]                      | 7.3            | 25.31 / 0.7719 / 0.282                                 |  | 25.27 / 0.7708 / 0.282                                 |  |
|                    | $C^2$ -Matching- $\ell_1$ [21] | 8.9            | 27.19 / 0.8402 / 0.362                                 |  | 27.23 / 0.8381 / 0.362                                 |  |
|                    | $C^2$ -Matching [21]           | 8.9            | 26.79 / 0.8141 / 0.327                                 |  | 26.81 / 0.8123 / 0.325                                 |  |
|                    | MASA- $\ell_1$ [30]            | 4.0            | 27.27 / 0.8372 / 0.339                                 |  | 27.30 / 0.8352 / 0.339                                 |  |
|                    | MASA [30]                      | 4.0            | 27.32 / 0.7640 / 0.273                                 |  | 27.37 / 0.7615 / 0.274                                 |  |
|                    | DCSR- $\ell_1$ [40]            | 3.2            | 27.73 / 0.8274 / 0.355                                 |  | 27.72 / 0.8275 / 0.349                                 |  |
|                    | DCSR [40]                      | 3.2            | 27.69 / 0.8232 / 0.276                                 |  | 27.68 / 0.8232 / 0.272                                 |  |
| Ours               | SelfDZSR- $\ell_1$             | 3.2            | <b>28.93 / 0.8572</b> / 0.308                          |  | <b>28.67 / 0.8457</b> / 0.328                          |  |
|                    | SelfDZSR                       | 3.2            | 28.67 / 0.8356 / <b>0.219</b>                          |  | 28.42 / 0.8238 / <b>0.231</b>                          |  |

## 4. Experiments

### 4.1. Experimental Setup

**Datasets.** Experiments are conducted on Nikon camera images from DRealSR dataset [44] and the CameraFusion dataset [40]. The training patches of DRealSR have been manually and carefully selected for mitigating the alignment issue, which is laborious and time-consuming. Instead, we take the original captured data without manual processing for training, making the whole process fully automated. In particular, each scene of the original data contains four different focal-length images. We adopt the longest focal-length image as the telephoto input and the shortest focal-length image as the short-focal input, which forms a  $\times 4$  DZSR dataset. There are 163 image pairs for training and 20 images for evaluation.

In the CameraFusion [40] dataset, the telephoto and short-focal images are from two lenses with different focal lengths of a smartphone. The focal length ratio between the telephoto and short-focal images is  $\sim 2$ . Thus, it can constitute a  $\times 2$  DZSR dataset. For this dataset, we use 112 image pairs for training and 12 images for evaluation.

**Data Pre-processing.** We first crop the center area of the short-focal image as LR. Then the brightness and color matching are employed between the LR and the telephoto images. Next, we use PWC-Net [37] to calculate the optical flow between the LR and the telephoto images, and warp the telephoto image. The warped telephoto image is used as GT and the center patch of it can be seen as Ref. Note that misalignment can still occur after registration, and our SelfDZSR is suggested to learn deep DZSR model while alleviating the adverse effect of misalignment.

**Training Configurations.** We augment the training data with random horizontal flip, vertical flip and  $90^\circ$  rotation. The batch size is 16, and the patch size for LR is  $48 \times 48$ . The model is trained with the Adam optimizer [23] by setting  $\beta_1 = 0.9$  and  $\beta_2 = 0.999$  for 400 epochs. The learning rate is initially set to  $1 \times 10^{-4}$  and is decayed to  $5 \times 10^{-5}$  after 200 epochs. The experiments are conducted with PyTorch [34] on an Nvidia GeForce RTX 2080Ti GPU.

**Evaluation Configurations.** There is no GT when inputting the original short-focus and telephoto images directly, so we also use the processed LR and Ref as input and warped telephoto as GT to compare the various methods by

Table 2. Quantitative results on CameraFusion dataset. We mark the best results in **bold**. The models trained only with  $\ell_1$  (or  $\ell_2$ ) loss are marked in gray. RefSR<sup>†</sup> represents that the RefSR methods are trained in our self-supervised learning manner.

|                    | Method                         | # Params<br>(M) | <i>Full-Image</i>                                      |  | <i>Corner-Image</i>                                    |  |
|--------------------|--------------------------------|-----------------|--|--|--|--|
|                    |                                |                 | PSNR $\uparrow$ / SSIM $\uparrow$ / LPIPS $\downarrow$ | PSNR $\uparrow$ / SSIM $\uparrow$ / LPIPS $\downarrow$ | PSNR $\uparrow$ / SSIM $\uparrow$ / LPIPS $\downarrow$ | PSNR $\uparrow$ / SSIM $\uparrow$ / LPIPS $\downarrow$ |
| SISR               | EDSR [28]                      | 43.1            | 25.43 / 0.8041 / 0.356                                 | 25.25 / 0.8007 / 0.349                                 | 25.25 / 0.8007 / 0.349                                 | 25.25 / 0.8007 / 0.349                                 |
|                    | RCAN [54]                      | 15.6            | 25.31 / 0.8034 / 0.355                                 | 25.14 / 0.8004 / 0.349                                 | 25.14 / 0.8004 / 0.349                                 | 25.14 / 0.8004 / 0.349                                 |
|                    | CDC [44]                       | 39.9            | 24.31 / 0.7811 / 0.380                                 | 24.11 / 0.7771 / 0.374                                 | 24.11 / 0.7771 / 0.374                                 | 24.11 / 0.7771 / 0.374                                 |
|                    | BSRGAN [50]                    | 16.7            | 25.09 / 0.7779 / 0.272                                 | 24.92 / 0.7749 / 0.266                                 | 24.92 / 0.7749 / 0.266                                 | 24.92 / 0.7749 / 0.266                                 |
|                    | Real-ESRGAN [41]               | 16.7            | 25.13 / 0.7788 / 0.261                                 | 24.90 / 0.7755 / 0.255                                 | 24.90 / 0.7755 / 0.255                                 | 24.90 / 0.7755 / 0.255                                 |
| RefSR <sup>†</sup> | SRNTT- $\ell_2$ [56]           | 5.5             | 24.78 / 0.7781 / 0.333                                 | 24.49 / 0.7737 / 0.331                                 | 24.49 / 0.7737 / 0.331                                 | 24.49 / 0.7737 / 0.331                                 |
|                    | SRNTT [56]                     | 5.5             | 23.69 / 0.7740 / 0.230                                 | 23.38 / 0.7700 / 0.229                                 | 23.38 / 0.7700 / 0.229                                 | 23.38 / 0.7700 / 0.229                                 |
|                    | TTSR- $\ell_1$ [49]            | 7.3             | 24.42 / 0.7937 / 0.375                                 | 24.12 / 0.7901 / 0.372                                 | 24.12 / 0.7901 / 0.372                                 | 24.12 / 0.7901 / 0.372                                 |
|                    | TTSR [49]                      | 7.3             | 23.05 / 0.7879 / 0.303                                 | 22.74 / 0.7854 / 0.300                                 | 22.74 / 0.7854 / 0.300                                 | 22.74 / 0.7854 / 0.300                                 |
|                    | $C^2$ -Matching- $\ell_1$ [21] | 8.9             | 25.24 / 0.7992 / 0.346                                 | 25.07 / 0.7971 / 0.340                                 | 25.07 / 0.7971 / 0.340                                 | 25.07 / 0.7971 / 0.340                                 |
|                    | $C^2$ -Matching [21]           | 8.9             | 24.18 / 0.7252 / 0.252                                 | 24.06 / 0.7254 / 0.245                                 | 24.06 / 0.7254 / 0.245                                 | 24.06 / 0.7254 / 0.245                                 |
|                    | MASA- $\ell_1$ [30]            | 4.0             | 25.78 / 0.8063 / 0.335                                 | 25.52 / 0.8026 / 0.331                                 | 25.52 / 0.8026 / 0.331                                 | 25.52 / 0.8026 / 0.331                                 |
|                    | MASA [30]                      | 4.0             | 25.42 / 0.7543 / 0.194                                 | 25.27 / 0.7524 / 0.190                                 | 25.27 / 0.7524 / 0.190                                 | 25.27 / 0.7524 / 0.190                                 |
|                    | DCSR- $\ell_1$ [40]            | 3.2             | 25.80 / 0.7974 / 0.300                                 | 25.48 / 0.7932 / 0.298                                 | 25.48 / 0.7932 / 0.298                                 | 25.48 / 0.7932 / 0.298                                 |
|                    | DCSR [40]                      | 3.2             | 25.51 / 0.7890 / 0.209                                 | 25.20 / 0.7847 / 0.211                                 | 25.20 / 0.7847 / 0.211                                 | 25.20 / 0.7847 / 0.211                                 |
| Ours               | SelfDZSR- $\ell_1$             | 3.2             | <b>26.35 / 0.8276</b> / 0.262                          | <b>25.67 / 0.8040</b> / 0.292                          | <b>25.67 / 0.8040</b> / 0.292                          | <b>25.67 / 0.8040</b> / 0.292                          |
|                    | SelfDZSR                       | 3.2             | 26.03 / 0.8008 / <b>0.158</b>                          | 25.37 / 0.7740 / <b>0.174</b>                          | 25.37 / 0.7740 / <b>0.174</b>                          | 25.37 / 0.7740 / <b>0.174</b>                          |

rule and line. Three common metrics on RGB channels are computed, *i.e.*, peak signal to noise ratio (PSNR), structural similarity (SSIM) [42] and learned perceptual image patch similarity (LPIPS) [52]. Noted that the scene of the Ref is the same as the center area of LR. In addition to calculating the metrics on the full image (marked as *Full-Image*), we also calculate the metrics of the area excluding the center (marked as *Corner-Image*). And all patches for visual comparison are selected from the area excluding the center of the whole image.

## 4.2. Results on Nikon Camera

We compare results with SISR (*i.e.*, EDSR [28], RCAN [54], CDC [44], BSRGAN [50] and Real-ESRGAN [41]) and RefSR (*i.e.*, SRNTT [56], TTSR [49], MASA [30],  $C^2$ -Matching [21] and DCSR [40]) methods. The results of BSRGAN and Real-ESRGAN are generated via the officially released model, other methods are retrained using our processed data for a fair comparison. Among them, RefSR methods are trained in our self-supervised learning manner and each method has two models, obtained by minimizing  $\ell_1$  (or  $\ell_2$ ) loss and all loss terms that are used in their papers.

Benefiting from the implicit alignment of the data pairs and better utilization of Ref information, SelfDZSR exceeds all competing methods on all metrics from Table 1. As shown in Fig. 6, our visual result restores much more details. More visual results and the evaluation of generalization capacity on other cameras will be given in the suppl.

## 4.3. Results on CameraFusion Dataset

Different from the Nikon camera images which scale factor of SR is  $\times 4$ , it is  $\times 2$  for the CameraFusion dataset.

Other settings of experiments on the CameraFusion dataset are the same as those on the Nikon camera images. Table 2 shows the comparison of quantitative results on the CameraFusion dataset, and we still achieve the best results among SISR and RefSR methods. The qualitative comparison will be given in the suppl.

## 5. Ablation Study

In this section, we conduct ablation experiments for assessing the effect of self-supervised learning, alignment methods and AdaSTN. Unless otherwise stated, experiments are carried out on the Nikon camera images [44], and the metrics are evaluated on full images.

### 5.1. Effect of Self-Supervised Learning

In order to verify the effectiveness of our proposed self-supervised approach, we conduct experiments on different training strategies. First, we remove the degradation module and AdaSTN of aligning LR with GT in SelfDZSR. Then we replace the real LR and pseudo-LR images with the bicubic downsampling HR image, and retrain the network. Finally, for a fair comparison, we take the self-supervised real-image adaptation (SRA) [40] and our self-supervised strategy to fine-tune the above model, respectively. As can be seen from Table 3 and Fig. 7, when evaluating on real-world images, our proposed self-supervised method achieves the better results. The PSNR metric is 0.27 dB higher than the model based on SRA fine-tuning. And our visual result is sharper and clearer.

Moreover, for the CameraFusion dataset, DCSR [40] model trained by our self-supervised approach obtains a 0.31 dB PSNR gain in comparison to the officially released



Figure 7. Visual comparison on training strategies. Our result in sub-figure (d) is sharper and clearer.

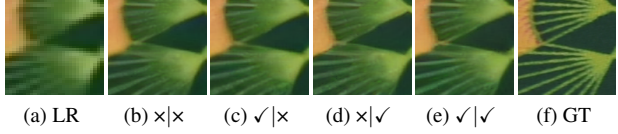


Figure 8. Visual comparison on alignment methods. The left and right sides of ‘|’ denote ‘align LR with pseudo-LR’ and ‘align Ref with pseudo-LR’, respectively. ‘×’ represents replacing pseudo-LR with LR. The lines in sub-figure (e) are more vivid.

Table 3. Ablation study on training strategies.

| Training Strategy    | PSNR $\uparrow$ | LPIPS $\downarrow$ |
|----------------------|-----------------|--------------------|
| Bicubic Degradation  | 28.07           | 0.398              |
| SRA Fine-tuning [40] | 28.26           | 0.278              |
| Our Fine-tuning      | 28.53           | 0.223              |

Table 4. Ablation study on alignment methods. Data pairs are pre-aligned by [37]. ‘×’ represents replacing pseudo-LR with LR.

| Align LR with pseudo-LR | Align Ref with pseudo-LR | PSNR $\uparrow$ | LPIPS $\downarrow$ |
|-------------------------|--------------------------|-----------------|--------------------|
| ×                       | ×                        | 28.48           | 0.222              |
| ✓                       | ×                        | 28.67           | 0.224              |
| ×                       | ✓                        | 28.61           | 0.220              |
| ✓                       | ✓                        | 28.67           | 0.219              |

model. In a word, it can be seen that even if the misalignment between LR and GT is not handled, our self-supervised method is still better than SRA [40] strategy.

## 5.2. Effect of Alignment

In order to evaluate the effect of our alignment methods, we experiment on the role of pseudo-LR in alignment by replacing pseudo-LR with LR during the training, which corresponds to Sec. 3.2 and Sec. 3.3. We consider the model that does not leverage pseudo-LR as the baseline, which also means that the training data is only pre-aligned by optical flow [37]. When aligning LR with pseudo-LR only, the PSNR increases by 0.19 dB against the baseline, as shown in Table 4. Coupled with the alignment between Ref and pseudo-LR, better quantitative and qualitative results can be further attained (see Fig. 8).

## 5.3. Effect of AdaSTN

We regard the model only using flow-based alignment [37] as the baseline. Then we modify the proposed AdaSTN to deformable convolution [7] and STN [20] to verify the effect of AdaSTN. For deformable convolution, instead of calculating the offset by estimating the affine



Figure 9. Visual comparison on the schemes of calculating offsets. ‘Deform’ represents deformable convolution. The oval shape in sub-figure (d) is more regular and clearer.

Table 5. Ablation study on AdaSTN.

| Method                         | PSNR $\uparrow$ | LPIPS $\downarrow$ |
|--------------------------------|-----------------|--------------------|
| Baseline                       | 28.48           | 0.222              |
| Baseline + Deformable Conv [7] | 28.52           | 0.225              |
| Baseline + STN [20]            | 28.57           | 0.219              |
| Baseline + AdaSTN              | 28.67           | 0.219              |

transformation matrix and vector according to Eqn. (5), we estimate the offset directly. For STN, we replace the pixel-level offset with a global affine transformation. The PSNR gain of taking AdaSTN is 0.15 dB compared with deformable convolution and 0.1 dB compared with STN, as shown in Table 5. And the visual results of using AdaSTN are visually more appealing, as shown in Fig. 9.

Meantime, for the image with the size of  $1445 \times 945$ , setting  $\mathbf{P} = \mathbf{0}$  (see Eqn. (5)) for AdaSTNs mentioned in Sec. 3.2 increases the average inference speed by  $\sim 0.2$  seconds without performance dropping.

## 6. Conclusion

Real-world image super-resolution from dual zoomed observations (DZSR) is an emerging topic, which aims to super-resolve the short focal length image with the reference of telephoto image. To circumvent the problem that ground-truth is unavailable, we present an effective self-supervised learning method, named SelfDZSR. To mitigate the adverse effect of image misalignment during training, pseudo-LR generating by degradation model and LR images are fed into proposed adaptive spatial transformer networks (AdaSTN) for implicit alignment. Experiments show that our proposed method can achieve better performance against the state-of-the-art methods both quantitatively and qualitatively.

## 7. Limitation, Impact, Etc

Similar to other RefSR methods, the main limitation of this work is the efficiency of calculating correlation. We will further study this issue in our future work. The proposed method can be embedded in imaging devices such as mobile phones, which can help obtain higher resolution images with more accurate details. And it has no foreseeable negative impact on society. We note that the images used in this work are from postcards or natural scenes. Thus, there are no ethical or privacy issues.



## Acknowledgement

This work was supported by Alibaba Group through Alibaba Innovative Research Program.

## References

- [1] Sefi Bell-Kligler, Assaf Shocher, and Michal Irani. Blind super-resolution kernel estimation using an internal-gan. In *NeurIPS*, pages 284–293, 2019. 2
- [2] Tim Brooks, Ben Mildenhall, Tianfan Xue, Jiawen Chen, Dillon Sharlet, and Jonathan T Barron. Unprocessing images for learned raw denoising. In *CVPR*, pages 11036–11045, 2019. 11
- [3] Jianrui Cai, Shuhang Gu, Radu Timofte, and Lei Zhang. Ntire 2019 challenge on real image super-resolution: Methods and results. In *CVPR Workshops*, pages 0–0, 2019. 3
- [4] Jianrui Cai, Hui Zeng, Hongwei Yong, Zisheng Cao, and Lei Zhang. Toward real-world single image super-resolution: A new benchmark and a new model. In *ICCV*, pages 3086–3095, 2019. 3
- [5] Kelvin CK Chan, Xintao Wang, Ke Yu, Chao Dong, and Chen Change Loy. Understanding deformable alignment in video super-resolution. In *AAAI*, pages 973–981, 2021. 2, 4
- [6] Chang Chen, Zhiwei Xiong, Xinmei Tian, Zheng-Jun Zha, and Feng Wu. Camera lens super-resolution. In *CVPR*, pages 1652–1660, 2019. 3
- [7] Jifeng Dai, Haozhi Qi, Yuwen Xiong, Yi Li, Guodong Zhang, Han Hu, and Yichen Wei. Deformable convolutional networks. In *ICCV*, pages 764–773, 2017. 2, 3, 5, 8
- [8] Mauricio Delbracio, Hossein Talebi, and Peyman Milanfar. Projected distribution loss for image enhancement. *arXiv preprint arXiv:2012.09289*, 2020. 5
- [9] Ishan Deshpande, Ziyu Zhang, and Alexander G Schwing. Generative modeling using the sliced wasserstein distance. In *CVPR*, pages 3483–3491, 2018. 5
- [10] Laurent Dinh, Jascha Sohl-Dickstein, and Samy Bengio. Density estimation using real nvp. In *ICLR*, 2017. 3
- [11] Chao Dong, Chen Change Loy, Kaiming He, and Xiaoou Tang. Image super-resolution using deep convolutional networks. *IEEE PAMI*, 38(2):295–307, 2015. 2
- [12] Alexey Dosovitskiy, Philipp Fischer, Eddy Ilg, Philip Hausser, Caner Hazirbas, Vladimir Golkov, Patrick Van Der Smagt, Daniel Cremers, and Thomas Brox. FlowNet: Learning optical flow with convolutional networks. In *ICCV*, pages 2758–2766, 2015. 3
- [13] Zigang Geng, Ke Sun, Bin Xiao, Zhaoxiang Zhang, and Jingdong Wang. Bottom-up human pose estimation via disentangled keypoint regression. In *CVPR*, pages 14676–14686, 2021. 5
- [14] Ian J Goodfellow, Jean Pouget-Abadie, Mehdi Mirza, Bing Xu, David Warde-Farley, Sherjil Ozair, Aaron C Courville, and Yoshua Bengio. Generative adversarial nets. In *NeurIPS*, 2014. 11
- [15] Jinjin Gu, Hannan Lu, Wangmeng Zuo, and Chao Dong. Blind super-resolution with iterative kernel correction. In *CVPR*, pages 1604–1613, 2019. 2
- [16] Kaiming He, Haoqi Fan, Yuxin Wu, Saining Xie, and Ross Girshick. Momentum contrast for unsupervised visual representation learning. In *CVPR*, pages 9729–9738, 2020. 3
- [17] Eric Heitz, Kenneth Vanhoey, Thomas Chambon, and Laurent Belcour. A sliced wasserstein loss for neural texture synthesis. In *CVPR*, pages 9412–9420, 2021. 5
- [18] Zheng Hui, Xinbo Gao, Yunchu Yang, and Xiumei Wang. Lightweight image super-resolution with information multi-distillation network. In *ACM MM*, pages 2024–2032, 2019. 2
- [19] Shady Abu Hussein, Tom Tirer, and Raja Giryes. Correction filter for single image super-resolution: Robustifying off-the-shelf deep super-resolvers. In *CVPR*, pages 1428–1437, 2020. 3
- [20] Max Jaderberg, Karen Simonyan, Andrew Zisserman, et al. Spatial transformer networks. In *NeurIPS*, pages 2017–2025, 2015. 5, 8
- [21] Yuming Jiang, Kelvin CK Chan, Xintao Wang, Chen Change Loy, and Ziwei Liu. Robust reference-based super-resolution via c2-matching. In *CVPR*, pages 2103–2112, 2021. 1, 2, 3, 5, 6, 7, 11, 13, 14, 15, 16, 17, 18
- [22] Alexia Jolicoeur-Martineau. The relativistic discriminator: a key element missing from standard gan. *arXiv preprint arXiv:1807.00734*, 2018. 11
- [23] Diederik P Kingma and Jimmy Ba. Adam: A method for stochastic optimization. In *ICLR*, 2015. 6
- [24] Xiangtao Kong, Hengyuan Zhao, Yu Qiao, and Chao Dong. Classsr: A general framework to accelerate super-resolution networks by data characteristic. In *CVPR*, pages 12016–12025, 2021. 2
- [25] Christian Ledig, Lucas Theis, Ferenc Huszár, Jose Caballero, Andrew Cunningham, Alejandro Acosta, Andrew Aitken, Alykhan Tejani, Johannes Totz, Zehan Wang, et al. Photo-realistic single image super-resolution using a generative adversarial network. In *CVPR*, pages 4681–4690, 2017. 2
- [26] Jingyun Liang, Guolei Sun, Kai Zhang, Luc Van Gool, and Radu Timofte. Mutual affine network for spatially variant kernel estimation in blind image super-resolution. In *ICCV*, pages 4096–4105, 2021. 3
- [27] Jingyun Liang, Kai Zhang, Shuhang Gu, Luc Van Gool, and Radu Timofte. Flow-based kernel prior with application to blind super-resolution. In *CVPR*, pages 10601–10610, 2021. 3
- [28] Bee Lim, Sanghyun Son, Heewon Kim, Seungjun Nah, and Kyoung Mu Lee. Enhanced deep residual networks for single image super-resolution. In *CVPR Workshops*, pages 136–144, 2017. 2, 5, 6, 7, 11, 13, 14, 15, 16
- [29] Ming Liu, Zhilu Zhang, Liya Hou, Wangmeng Zuo, and Lei Zhang. Deep adaptive inference networks for single image super-resolution. In *ECCV Workshops*, pages 131–148. Springer, 2020. 2
- [30] Liying Lu, Wenbo Li, Xin Tao, Jiangbo Lu, and Jiaya Jia. Masa-sr: Matching acceleration and spatial adaptation for reference-based image super-resolution. In *CVPR*, pages 6368–6377, 2021. 1, 2, 3, 6, 7, 11, 13, 14, 15, 16, 17, 18
- [31] Andreas Lugmayr, Martin Danelljan, and Radu Timofte. Ntire 2020 challenge on real-world image super-resolution:

- Methods and results. In *CVPR Workshops*, pages 494–495, 2020. 3
- [32] Andreas Lugmayr, Martin Danelljan, Radu Timofte, Manuel Fritsche, Shuhang Gu, Kuldeep Purohit, Praveen Kandula, Maitreya Suin, AN Rajagoapalan, Nam Hyung Joon, et al. Aim 2019 challenge on real-world image super-resolution: Methods and results. In *ICCV Workshops*, pages 3575–3583. IEEE, 2019. 3
- [33] Zhengxiong Luo, Yan Huang, Shang Li, Liang Wang, and Tieniu Tan. Unfolding the alternating optimization for blind super resolution. In *NeurIPS*, 2020. 2
- [34] Adam Paszke, Sam Gross, Francisco Massa, Adam Lerer, James Bradbury, Gregory Chanan, Trevor Killeen, Zeming Lin, Natalia Gimelshein, Luca Antiga, Alban Desmaison, Andreas Kopf, Edward Yang, Zachary DeVito, Martin Raison, Alykhan Tejani, Sasank Chilamkurthy, Benoit Steiner, Lu Fang, Junjie Bai, and Soumith Chintala. Pytorch: An imperative style, high-performance deep learning library. In *NeurIPS*, pages 8024–8035, 2019. 6
- [35] Gyumin Shim, Jinsun Park, and In So Kweon. Robust reference-based super-resolution with similarity-aware deformable convolution. In *CVPR*, pages 8425–8434, 2020. 1, 3
- [36] Karen Simonyan and Andrew Zisserman. Very deep convolutional networks for large-scale image recognition. In *ICLR*, 2014. 5, 11
- [37] Deqing Sun, Xiaodong Yang, Ming-Yu Liu, and Jan Kautz. Pwc-net: Cnns for optical flow using pyramid, warping, and cost volume. In *CVPR*, pages 8934–8943, 2018. 2, 3, 4, 6, 8
- [38] Longguang Wang, Xiaoyu Dong, Yingqian Wang, Xinyi Ying, Zaiping Lin, Wei An, and Yulan Guo. Exploring sparsity in image super-resolution for efficient inference. In *CVPR*, pages 4917–4926, 2021. 2
- [39] Longguang Wang, Yingqian Wang, Xiaoyu Dong, Qingyu Xu, Jungang Yang, Wei An, and Yulan Guo. Unsupervised degradation representation learning for blind super-resolution. In *CVPR*, pages 10581–10590, 2021. 3
- [40] Tengfei Wang, Jiaxin Xie, Wenxiu Sun, Qiong Yan, and Qifeng Chen. Dual-camera super-resolution with aligned attention modules. In *ICCV*, pages 2001–2010, 2021. 2, 3, 6, 7, 8, 11, 12, 13, 14, 15, 16, 17, 18
- [41] Xintao Wang, Liangbin Xie, Chao Dong, and Ying Shan. Real-esrgan: Training real-world blind super-resolution with pure synthetic data. In *ICCV Workshops*, pages 1905–1914, 2021. 3, 6, 7, 11, 13, 14, 15, 16, 17, 18
- [42] Zhou Wang, Alan C Bovik, Hamid R Sheikh, and Eero P Simoncelli. Image quality assessment: from error visibility to structural similarity. *IEEE TIP*, 13(4):600–612, 2004. 7
- [43] Pengxu Wei, Hannan Lu, Radu Timofte, Liang Lin, Wangmeng Zuo, Zhihong Pan, Baopu Li, Teng Xi, Yanwen Fan, Gang Zhang, et al. Aim 2020 challenge on real image super-resolution: methods and results. In *ECCV Workshops*, pages 392–422. Springer, 2020. 3
- [44] Pengxu Wei, Ziwei Xie, Hannan Lu, Zongyuan Zhan, Qixiang Ye, Wangmeng Zuo, and Liang Lin. Component divide-and-conquer for real-world image super-resolution. In *ECCV*, pages 101–117. Springer, 2020. 2, 3, 6, 7, 11, 12, 13, 14, 15, 16
- [45] Yunxuan Wei, Shuhang Gu, Yawei Li, Radu Timofte, Longcun Jin, and Hengjie Song. Unsupervised real-world image super resolution via domain-distance aware training. In *CVPR*, pages 13385–13394, 2021. 3
- [46] Jiqing Wu, Zhiwu Huang, Dinesh Acharya, Wen Li, Janine Thoma, Danda Pani Paudel, and Luc Van Gool. Sliced wasserstein generative models. In *CVPR*, pages 3713–3722, 2019. 5
- [47] Wenbin Xie, Dehua Song, Chang Xu, Chunjing Xu, Hui Zhang, and Yunhe Wang. Learning frequency-aware dynamic network for efficient super-resolution. In *ICCV*, pages 4308–4317, 2021. 2
- [48] Yanchun Xie, Jimin Xiao, Mingjie Sun, Chao Yao, and Kaizhu Huang. Feature representation matters: End-to-end learning for reference-based image super-resolution. In *ECCV*, pages 230–245. Springer, 2020. 1, 3
- [49] Fuzhi Yang, Huan Yang, Jianlong Fu, Hongtao Lu, and Bain-ing Guo. Learning texture transformer network for image super-resolution. In *CVPR*, pages 5791–5800, 2020. 1, 2, 3, 6, 7, 11, 13, 14, 15, 16, 17, 18
- [50] Kai Zhang, Jingyun Liang, Luc Van Gool, and Radu Timofte. Designing a practical degradation model for deep blind image super-resolution. In *ICCV*, pages 4791–4800, 2021. 3, 6, 7, 11, 13, 14, 15, 16, 17, 18
- [51] Kai Zhang, Wangmeng Zuo, and Lei Zhang. Learning a single convolutional super-resolution network for multiple degradations. In *CVPR*, pages 3262–3271, 2018. 2
- [52] Richard Zhang, Phillip Isola, Alexei A Efros, Eli Shechtman, and Oliver Wang. The unreasonable effectiveness of deep features as a perceptual metric. In *CVPR*, pages 586–595, 2018. 6, 7
- [53] Xuaner Zhang, Qifeng Chen, Ren Ng, and Vladlen Koltun. Zoom to learn, learn to zoom. In *CVPR*, pages 3762–3770, 2019. 3
- [54] Yulun Zhang, Kunpeng Li, Kai Li, Lichen Wang, Bineng Zhong, and Yun Fu. Image super-resolution using very deep residual channel attention networks. In *ECCV*, pages 286–301, 2018. 2, 6, 7, 11, 13, 14, 15, 16
- [55] Zhilu Zhang, Haolin Wang, Ming Liu, Ruohao Wang, Jiawei Zhang, and Wangmeng Zuo. Learning raw-to-srgb mappings with inaccurately aligned supervision. In *ICCV*, pages 4348–4358, 2021. 2, 3, 4
- [56] Zhifei Zhang, Zhaowen Wang, Zhe Lin, and Hairong Qi. Image super-resolution by neural texture transfer. In *CVPR*, pages 7982–7991, 2019. 1, 2, 3, 6, 7, 11, 13, 14, 15, 16, 17, 18
- [57] Haitian Zheng, Mengqi Ji, Lei Han, Ziwei Xu, Haoqian Wang, Yebin Liu, and Lu Fang. Learning cross-scale correspondence and patch-based synthesis for reference-based super-resolution. In *BMVC*, volume 1, page 2, 2017. 3
- [58] Haitian Zheng, Mengqi Ji, Haoqian Wang, Yebin Liu, and Lu Fang. Crossnet: An end-to-end reference-based super resolution network using cross-scale warping. In *ECCV*, pages 88–104, 2018. 3
- [59] Xizhou Zhu, Han Hu, Stephen Lin, and Jifeng Dai. Deformable convnets v2: More deformable, better results. In *CVPR*, pages 9308–9316, 2019. 3

# Supplementary Material

## A. Content

The content of this supplementary material involves:

- Synthetic noise of degradation model in Sec. B.
- Network structure of restoration module in Sec. C.
- Sliced Wasserstein (SW) loss in Sec. D.
- Evaluation of generalization performance on other cameras in Sec. E.
- Additional visual comparison on Nikon camera and CameraFusion dataset in Sec. F.

## B. Synthetic Noise of Degradation Model

Noise in real-world images is common, but complex and various. In order to bridge the gap between pseudo-LR and LR as much as possible, we need to add noise to the output of the degradation network that only simulates the blurring and down-sampling processes. Gaussian noise is a natural choice, but much different from real-world image noise. Inspired by BSRGAN [50], we also add JPEG compression noise and processed camera sensor noise [2]. The variance of Gaussian noise is uniformly sampled from 5/255 to 30/255, and the JPEG quality factor is uniformly chosen from 60 to 95. Simultaneously, the order of adding three kinds of noise is stochastic.

## C. Restoration Module

Fig. A(a) shows the detailed structure of the restoration module. First, the aligned LR and aligned Ref features are concatenated and fed into the backbone, which consists of 16 residual blocks [28]. Then the concatenated features are input into an encoder for generating vectors that modulate the features of each residual block. Simultaneously, the original Ref image and the central area of the LR image are utilized to enrich the input features of the encoder for better modulation. This modulation can also be regarded as a kind of channel attention on the features of residual block. And it is beneficial to relieve the color inconsistency (see Fig. A(b)) between the short focal length and telephoto images in the real world.

## D. Sliced Wasserstein Loss

The algorithm of SW loss is given in Alg. A. We first obtain the 1-dimensional representation of 2-dimensional VGG [36] features through random linear projection. Then we calculate the Wasserstein distance between the output and the target 1-dimensional probability distributions,

which is defined as the element-wise  $\ell_1$  distance over sorted 1-dimensional distributions.

Most reference-based image SR (RefSR) methods [21, 30, 49, 56] adopt the perceptual loss and adversarial loss [14] for more realistic results. For a fair comparison, here we also train proposed model (SelfDZSR) using a combination of  $\ell_1$  reconstruction loss, perceptual loss and adversarial loss based on Relativistic GAN [22]. The quantitative results are shown in Table A. It can be seen that the model trained by SW loss obtains a 0.22 dB PSNR gain than that by adversarial loss, while the gap of LPIPS metric is small. Nevertheless, benefiting from the proposed implicit alignment and better utilization of Ref information, the SelfDZSR model by adversarial loss still achieves better performance than other RefSR methods.

Table A. Quantitative results of SelfSZSR using different loss terms.

| Loss Terms                          | PSNR $\uparrow$ | LPIPS $\downarrow$ |
|-------------------------------------|-----------------|--------------------|
| $\ell_1$                            | 28.93           | 0.308              |
| $\ell_1$ + SW                       | 28.67           | 0.219              |
| $\ell_1$ + Perceptual + Adversarial | 28.45           | 0.216              |

## E. Evaluation of Generalization Performance on Other Cameras

Here we evaluate the generalization performance of models on other four cameras (*i.e.*, Canon, Olympus, Panasonic and Sony) from DRealSR dataset [44]. We compare results with SISR (*i.e.*, EDSR<sup>1</sup> [28], RCAN<sup>2</sup> [54], CDC<sup>3</sup> [44], BSRGAN<sup>4</sup> [50] and Real-ESRGAN<sup>5</sup> [41]) and RefSR (*i.e.*, SRNTT<sup>6</sup> [56], TTSTR<sup>7</sup> [49], MASA<sup>8</sup> [30], C<sup>2</sup>-Matching<sup>9</sup> [21] and DCSR<sup>10</sup> [40]) methods. Among them, the results of BSRGAN and Real-ESRGAN are generated via the officially released model while other methods are trained on Nikon camera images, as mentioned in the main text of the submission.

<sup>1</sup><https://github.com/sanghyun-son/EDSR-PyTorch>

<sup>2</sup><https://github.com/yulunzhang/RCAN>

<sup>3</sup><https://github.com/xiezw5/Component-Divide-and-Conquer-for-Real-World-Image-Super-Resolution>

<sup>4</sup><https://github.com/cszn/BSRGAN>

<sup>5</sup><https://github.com/xinntao/Real-ESRGAN>

<sup>6</sup><https://github.com/S-aiueo32/srntt-pytorch>

<sup>7</sup><https://github.com/researchmm/TTSTR>

<sup>8</sup><https://github.com/dvlab-research/MASA-SR>

<sup>9</sup><https://github.com/yumingj/C2-Matching>

<sup>10</sup><https://github.com/Tengfei-Wang/DCSR>

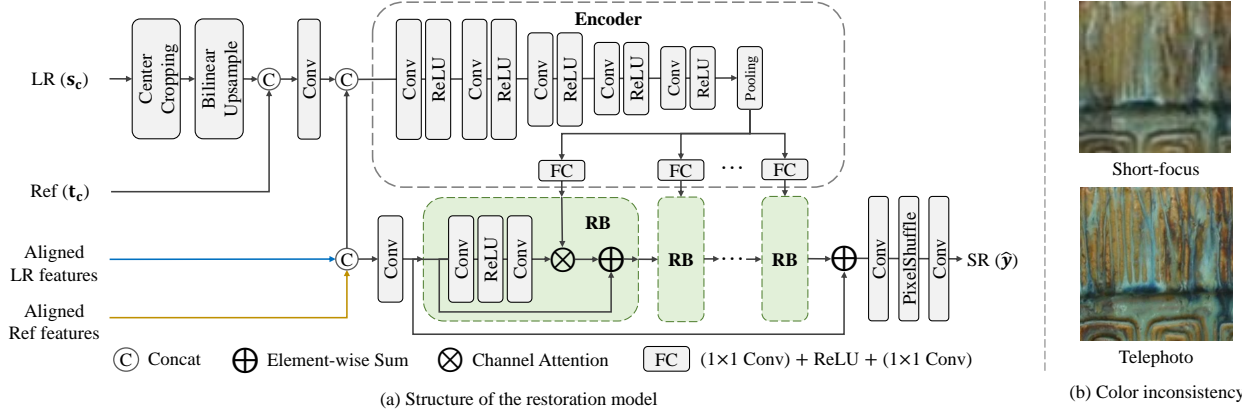


Figure A. Structure of the restoration model and color inconsistency. (a) Detailed structure of the restoration model. ‘RB’ denotes the residual block. The colors of lines correspond to Fig. 3 in the submitted manuscript. (b) Color inconsistency between short-focus and telephoto images.

---

#### Algorithm A Pseudocode of SW loss

---

**Require:**  $\mathbf{U} \in \mathbb{R}^{C \times H \times W}$ : VGG features of output image;  $\mathbf{V} \in \mathbb{R}^{C \times H \times W}$ : VGG features of target image;  $\mathbf{M} \in \mathbb{R}^{C' \times C}$ : random projection matrix;

**Ensure:**  $\mathcal{L}_{\text{SW}}(\mathbf{U}, \mathbf{V})$ : the value of SW loss;

- 1: flatten features  $\mathbf{U}$  and  $\mathbf{V}$  to  $\mathbf{U}_f (\in \mathbb{R}^{C \times HW})$  and  $\mathbf{V}_f (\in \mathbb{R}^{C \times HW})$ , respectively;
  - 2: project the features onto  $C'$  directions:  $\mathbf{U}_p = \mathbf{M}\mathbf{U}_f$ ,  $\mathbf{V}_p = \mathbf{M}\mathbf{V}_f$ ;
  - 3: sort projections for each direction:  $\mathbf{U}_s = \text{Sort}(\mathbf{U}_p, \text{dim}=1)$ ,  $\mathbf{V}_s = \text{Sort}(\mathbf{V}_p, \text{dim}=1)$ ;
  - 4:  $\mathcal{L}_{\text{SW}}(\mathbf{U}, \mathbf{V}) = \|\mathbf{U}_s - \mathbf{V}_s\|_1$
- 

Tables B~E show the quantitative results on four cameras, respectively. Our proposed model (SelfDZSR) achieves better results than most other methods, especially on *Full-Image* and LPIPS metric. The visual comparison is carried out on the methods that are trained not only with  $\ell_1$  (or  $\ell_2$ ) loss. The comparisons on four cameras can be seen in Fig. B~E, respectively.

## F. Additional Visual Comparison on Nikon Camera and CameraFusion Dataset

The visual comparison is carried out on the methods that are trained not only with  $\ell_1$  (or  $\ell_2$ ) loss. In Fig. F, we show more qualitative comparison on Nikon camera images [44]. The visual comparison on CameraFusion dataset [40] can be seen in Fig. G. The resolution of full LR images from the two test sets is 1~2K, so we select a patch for comparison.



Table B. Quantitative results on **Canon** camera with 17 images. We mark the best results in **bold**. The models trained only with  $\ell_1$  (or  $\ell_2$ ) loss are marked in gray. RefSR<sup>†</sup> represents that the RefSR methods are trained in our self-supervised learning manner.

|                    | Method                         | # Param<br>(M) | <i>Full-Image</i>                                      |                               | <i>Corner-Image</i>                                    |  |
|--------------------|--------------------------------|----------------|--|-------------------------------|--|--|
|                    |                                |                | PSNR $\uparrow$ / SSIM $\uparrow$ / LPIPS $\downarrow$ |                               | PSNR $\uparrow$ / SSIM $\uparrow$ / LPIPS $\downarrow$ |  |
| SISR               | EDSR [28]                      | 43.1           | 26.52 / 0.8399 / 0.342                                 | 26.55 / 0.8383 / 0.342        |  |  |
|                    | RCAN [54]                      | 15.6           | 26.69 / 0.8413 / 0.346                                 | 26.73 / 0.8404 / 0.347        |  |  |
|                    | CDC [44]                       | 39.9           | 24.85 / 0.8378 / 0.384                                 | 24.90 / 0.8366 / 0.385        |  |  |
|                    | BSRGAN [50]                    | 16.7           | 25.39 / 0.8031 / 0.268                                 | 25.43 / 0.8017 / 0.268        |  |  |
|                    | Real-ESRGAN [41]               | 16.7           | 24.64 / 0.8010 / 0.275                                 | 24.68 / 0.7988 / 0.276        |  |  |
| RefSR <sup>†</sup> | SRNTT- $\ell_2$ [56]           | 5.5            | 26.22 / 0.8390 / 0.348                                 | 26.24 / 0.8378 / 0.351        |  |  |
|                    | SRNTT [56]                     | 5.5            | 26.25 / 0.8268 / 0.295                                 | 26.28 / 0.8258 / 0.293        |  |  |
|                    | TTSR- $\ell_1$ [49]            | 7.3            | 23.97 / 0.8280 / 0.374                                 | 23.93 / 0.8259 / 0.375        |  |  |
|                    | TTSR [49]                      | 7.3            | 23.75 / 0.7719 / 0.340                                 | 23.68 / 0.7695 / 0.338        |  |  |
|                    | $C^2$ -Matching- $\ell_1$ [21] | 8.9            | 25.64 / 0.8383 / 0.357                                 | 25.60 / 0.8373 / 0.358        |  |  |
|                    | $C^2$ -Matching [21]           | 8.9            | 24.75 / 0.8180 / 0.329                                 | 24.72 / 0.8171 / 0.328        |  |  |
|                    | MASA- $\ell_1$ [30]            | 4.0            | 26.54 / 0.8398 / 0.338                                 | 26.58 / 0.8390 / 0.339        |  |  |
|                    | MASA [30]                      | 4.0            | 27.19 / 0.8006 / 0.306                                 | 27.24 / 0.7994 / 0.305        |  |  |
|                    | DCSR- $\ell_1$ [40]            | 3.2            | 27.55 / 0.8363 / 0.338                                 | 27.54 / 0.8377 / 0.330        |  |  |
|                    | DCSR [40]                      | 3.2            | 26.80 / 0.8265 / 0.275                                 | 26.79 / 0.8275 / 0.268        |  |  |
| Ours               | SelfDZSR- $\ell_1$             | 3.2            | <b>28.13 / 0.8576 / 0.300</b>                          | <b>27.87 / 0.8465 / 0.321</b> |  |  |
|                    | SelfDZSR                       | 3.2            | 27.85 / 0.8386 / <b>0.240</b>                          | 27.60 / 0.8274 / <b>0.253</b> |  |  |

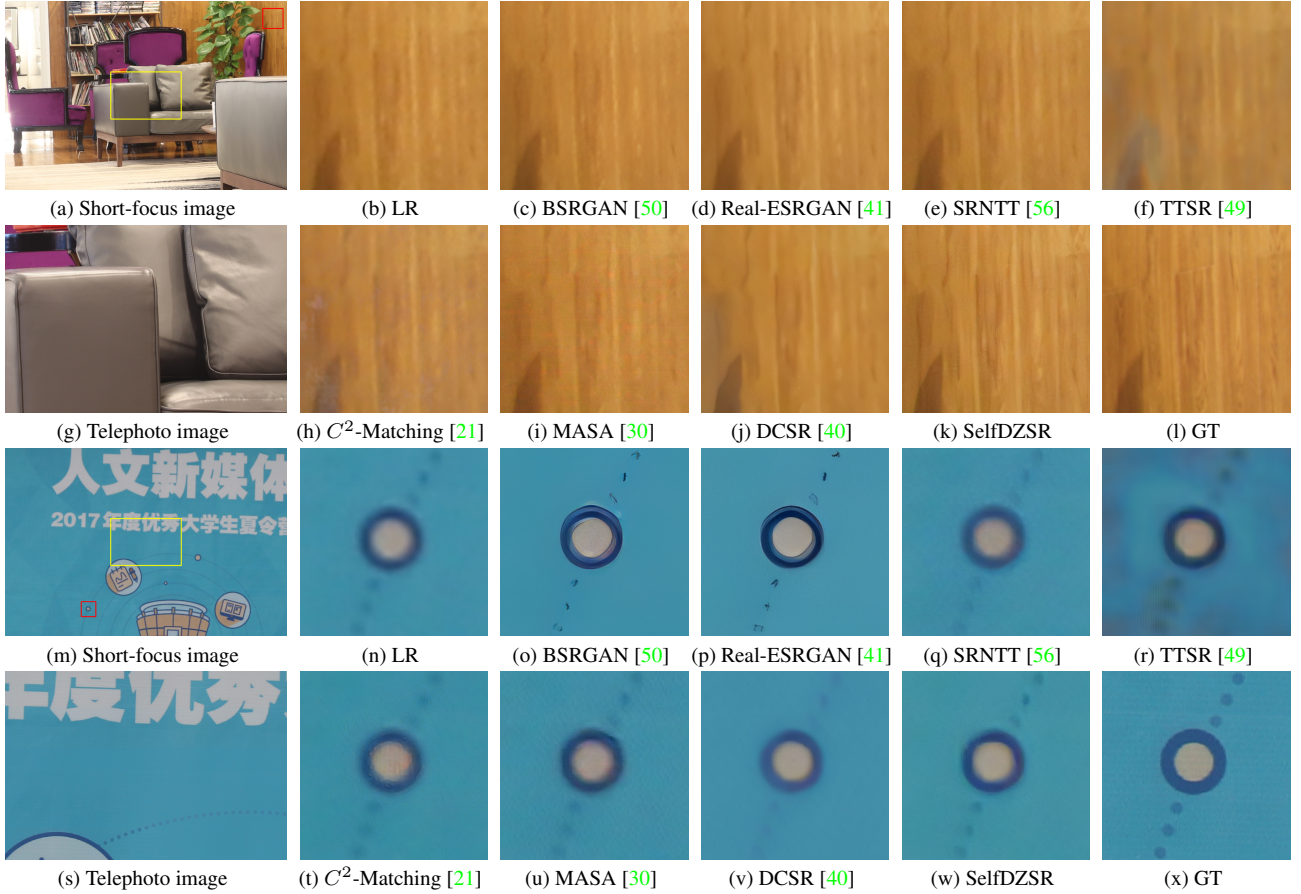


Figure B. Visual comparison on **Canon** camera. In the short-focus image, the yellow box indicates the overlapped scene with the telephoto image, while the red box represents the selected LR patch. Our result in sub-figure (k) restores more fine-scale textures, and that in sub-figure (w) is clearer and more photo-realistic.

Table C. Quantitative results on **Olympus** camera with 19 images. We mark the best results in **bold**. The models trained only with  $\ell_1$  (or  $\ell_2$ ) loss are marked in gray. RefSR<sup>†</sup> represents that the RefSR methods are trained in our self-supervised learning manner.

|                    | Method                         | # Param<br>(M) | <i>Full-Image</i>                    |                               |                               | <i>Corner-Image</i>           |                               |                               |
|--------------------|--------------------------------|----------------|--------------------------------------|-------------------------------|-------------------------------|-------------------------------|-------------------------------|-------------------------------|
|                    |                                |                | PSNR↑ / SSIM↑ / LPIPS↓               | PSNR↑ / SSIM↑ / LPIPS↓        | PSNR↑ / SSIM↑ / LPIPS↓        | PSNR↑ / SSIM↑ / LPIPS↓        | PSNR↑ / SSIM↑ / LPIPS↓        | PSNR↑ / SSIM↑ / LPIPS↓        |
| SISR               | EDSR [28]                      | 43.1           | 26.99 / 0.7960 / 0.452               | 26.99 / 0.7917 / 0.451        | 26.99 / 0.7917 / 0.451        | 26.99 / 0.7917 / 0.451        | 26.99 / 0.7917 / 0.451        | 26.99 / 0.7917 / 0.451        |
|                    | RCAN [54]                      | 15.6           | 27.54 / 0.8038 / 0.452               | 27.54 / 0.7995 / 0.451        | 27.54 / 0.7995 / 0.451        | 27.54 / 0.7995 / 0.451        | 27.54 / 0.7995 / 0.451        | 27.54 / 0.7995 / 0.451        |
|                    | CDC [44]                       | 39.9           | 27.31 / 0.8030 / 0.466               | 27.30 / 0.7988 / 0.467        | 27.30 / 0.7988 / 0.467        | 27.30 / 0.7988 / 0.467        | 27.30 / 0.7988 / 0.467        | 27.30 / 0.7988 / 0.467        |
|                    | BSRGAN [50]                    | 16.7           | 25.76 / 0.7422 / 0.341               | 25.75 / 0.7388 / 0.341        | 25.75 / 0.7388 / 0.341        | 25.75 / 0.7388 / 0.341        | 25.75 / 0.7388 / 0.341        | 25.75 / 0.7388 / 0.341        |
|                    | Real-ESRGAN [41]               | 16.7           | 26.00 / 0.7545 / 0.323               | 25.98 / 0.7517 / 0.321        | 25.98 / 0.7517 / 0.321        | 25.98 / 0.7517 / 0.321        | 25.98 / 0.7517 / 0.321        | 25.98 / 0.7517 / 0.321        |
| RefSR <sup>†</sup> | SRNTT- $\ell_2$ [56]           | 5.5            | 26.51 / 0.7928 / 0.442               | 26.49 / 0.7879 / 0.441        | 26.49 / 0.7879 / 0.441        | 26.49 / 0.7879 / 0.441        | 26.49 / 0.7879 / 0.441        | 26.49 / 0.7879 / 0.441        |
|                    | SRNTT [56]                     | 5.5            | 27.04 / 0.7870 / 0.357               | 27.03 / 0.7823 / 0.354        | 27.03 / 0.7823 / 0.354        | 27.03 / 0.7823 / 0.354        | 27.03 / 0.7823 / 0.354        | 27.03 / 0.7823 / 0.354        |
|                    | TTSR- $\ell_1$ [49]            | 7.3            | 25.44 / 0.7790 / 0.469               | 25.39 / 0.7756 / 0.466        | 25.39 / 0.7756 / 0.466        | 25.39 / 0.7756 / 0.466        | 25.39 / 0.7756 / 0.466        | 25.39 / 0.7756 / 0.466        |
|                    | TTSR [49]                      | 7.3            | 25.12 / 0.7736 / 0.377               | 25.08 / 0.7693 / 0.370        | 25.08 / 0.7693 / 0.370        | 25.08 / 0.7693 / 0.370        | 25.08 / 0.7693 / 0.370        | 25.08 / 0.7693 / 0.370        |
|                    | $C^2$ -Matching- $\ell_1$ [21] | 8.9            | 26.65 / 0.8001 / 0.448               | 26.62 / 0.7960 / 0.446        | 26.62 / 0.7960 / 0.446        | 26.62 / 0.7960 / 0.446        | 26.62 / 0.7960 / 0.446        | 26.62 / 0.7960 / 0.446        |
|                    | $C^2$ -Matching [21]           | 8.9            | 26.51 / 0.7728 / 0.380               | 26.49 / 0.7682 / 0.378        | 26.49 / 0.7682 / 0.378        | 26.49 / 0.7682 / 0.378        | 26.49 / 0.7682 / 0.378        | 26.49 / 0.7682 / 0.378        |
|                    | MASA- $\ell_1$ [30]            | 4.0            | 27.17 / 0.7982 / 0.423               | 27.17 / 0.7937 / 0.423        | 27.17 / 0.7937 / 0.423        | 27.17 / 0.7937 / 0.423        | 27.17 / 0.7937 / 0.423        | 27.17 / 0.7937 / 0.423        |
|                    | MASA [30]                      | 4.0            | 26.66 / 0.7393 / 0.351               | 26.66 / 0.7348 / 0.350        | 26.66 / 0.7348 / 0.350        | 26.66 / 0.7348 / 0.350        | 26.66 / 0.7348 / 0.350        | 26.66 / 0.7348 / 0.350        |
|                    | DCSR- $\ell_1$ [40]            | 3.2            | 27.74 / 0.7987 / 0.437               | <b>27.73</b> / 0.7973 / 0.426 | <b>27.73</b> / 0.7973 / 0.426 | <b>27.73</b> / 0.7973 / 0.426 | <b>27.73</b> / 0.7973 / 0.426 | <b>27.73</b> / 0.7973 / 0.426 |
|                    | DCSR [40]                      | 3.2            | 27.41 / 0.7894 / 0.351               | 27.39 / 0.7882 / 0.342        | 27.39 / 0.7882 / 0.342        | 27.39 / 0.7882 / 0.342        | 27.39 / 0.7882 / 0.342        | 27.39 / 0.7882 / 0.342        |
| Ours               | SelfDZSR- $\ell_1$             | 3.2            | <b>27.79</b> / <b>0.8124</b> / 0.395 | 27.56 / <b>0.7980</b> / 0.420 | 27.56 / <b>0.7980</b> / 0.420 | 27.56 / <b>0.7980</b> / 0.420 | 27.56 / <b>0.7980</b> / 0.420 | 27.56 / <b>0.7980</b> / 0.420 |
|                    | SelfDZSR                       | 3.2            | 27.34 / 0.7862 / <b>0.292</b>        | 27.12 / 0.7722 / <b>0.310</b> | 27.12 / 0.7722 / <b>0.310</b> | 27.12 / 0.7722 / <b>0.310</b> | 27.12 / 0.7722 / <b>0.310</b> | 27.12 / 0.7722 / <b>0.310</b> |

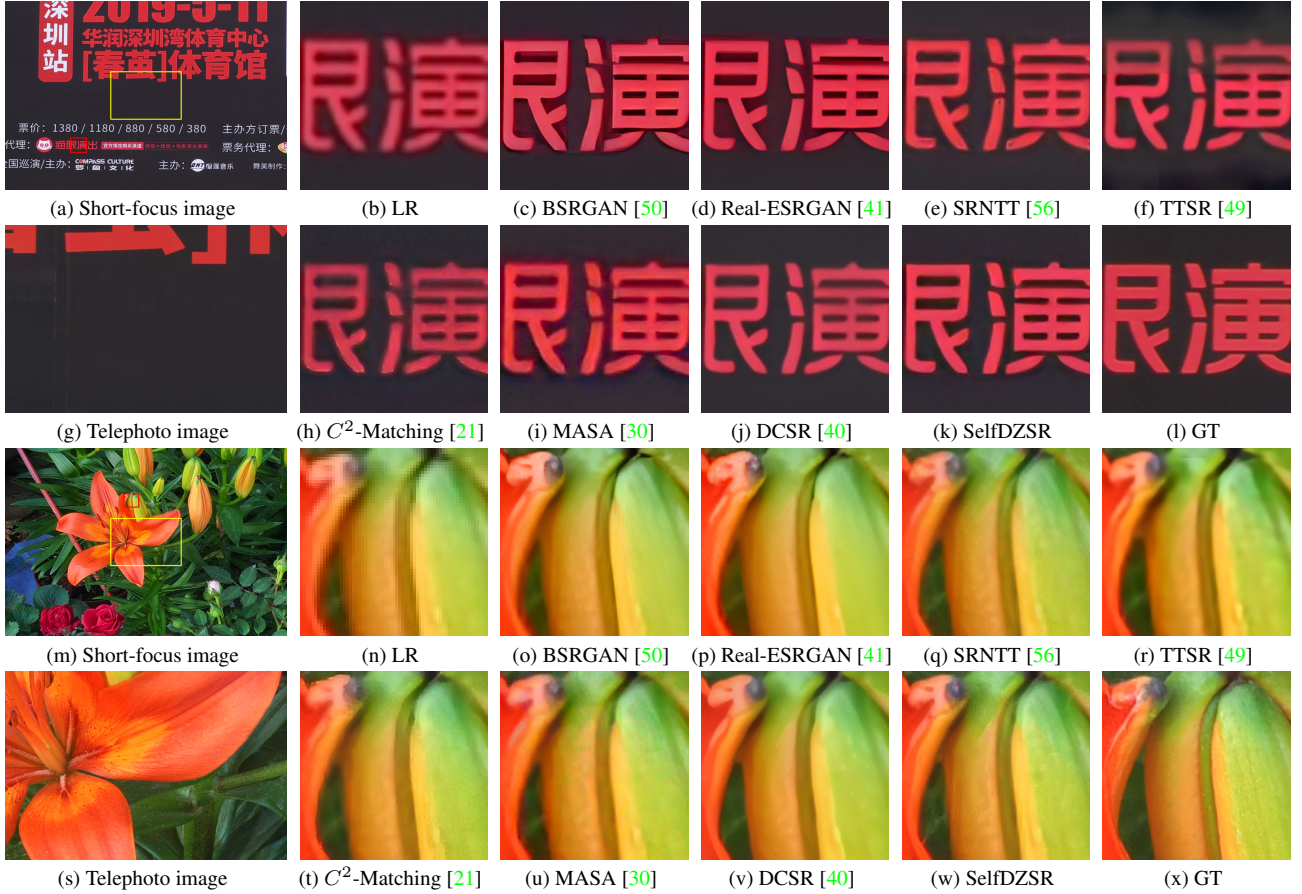


Figure C. Visual comparison on **Olympus** camera. In the short-focus image, the yellow box indicates the overlapped scene with the telephoto image, while the red box represents the selected LR patch. Our result in sub-figure (k) is clearer, and that in sub-figure (w) is more photo-realistic.



Table D. Quantitative results on **Panasonic** camera with 20 images. We mark the best results in **bold**. The models trained only with  $\ell_1$  (or  $\ell_2$ ) loss are marked in gray. RefSR<sup>†</sup> represents that the RefSR methods are trained in our self-supervised learning manner.

|                    | Method                         | # Param<br>(M) | <i>Full-Image</i>                                      | <i>Corner-Image</i>                                    |
|--------------------|--------------------------------|----------------|--|--|
|                    |                                |                | PSNR $\uparrow$ / SSIM $\uparrow$ / LPIPS $\downarrow$ | PSNR $\uparrow$ / SSIM $\uparrow$ / LPIPS $\downarrow$ |
| SISR               | EDSR [28]                      | 43.1           | 27.04 / 0.7994 / 0.379                                 | 27.15 / 0.7964 / 0.380                                 |
|                    | RCAN [54]                      | 15.6           | 27.26 / 0.8055 / 0.381                                 | 27.36 / 0.8027 / 0.383                                 |
|                    | CDC [44]                       | 39.9           | 27.02 / 0.7981 / 0.414                                 | 27.12 / 0.7949 / 0.414                                 |
|                    | BSRGAN [50]                    | 16.7           | 26.27 / 0.7520 / 0.288                                 | 26.40 / 0.7482 / 0.288                                 |
|                    | Real-ESRGAN [41]               | 16.7           | 26.20 / 0.7625 / 0.275                                 | 26.31 / 0.7592 / 0.274                                 |
| RefSR <sup>†</sup> | SRNTT- $\ell_2$ [56]           | 5.5            | 27.08 / 0.7988 / 0.374                                 | 27.18 / 0.7960 / 0.375                                 |
|                    | SRNTT [56]                     | 5.5            | 27.14 / 0.7862 / 0.307                                 | 27.22 / 0.7829 / 0.306                                 |
|                    | TTSR- $\ell_1$ [49]            | 7.3            | 26.21 / 0.7859 / 0.383                                 | 26.26 / 0.7842 / 0.385                                 |
|                    | TTSR [49]                      | 7.3            | 25.24 / 0.7558 / 0.329                                 | 25.26 / 0.7537 / 0.326                                 |
|                    | $C^2$ -Matching- $\ell_1$ [21] | 8.9            | 26.61 / 0.8032 / 0.378                                 | 26.71 / 0.7994 / 0.381                                 |
|                    | $C^2$ -Matching [21]           | 8.9            | 25.70 / 0.7649 / 0.340                                 | 25.78 / 0.7596 / 0.342                                 |
|                    | MASA- $\ell_1$ [30]            | 4.0            | 26.94 / 0.7997 / 0.363                                 | 27.00 / 0.7958 / 0.365                                 |
|                    | MASA [30]                      | 4.0            | 26.93 / 0.7388 / 0.299                                 | 27.04 / 0.7365 / 0.299                                 |
|                    | DCSR- $\ell_1$ [40]            | 3.2            | 26.58 / 0.7640 / 0.398                                 | 26.54 / 0.7632 / 0.390                                 |
|                    | DCSR [40]                      | 3.2            | 26.40 / 0.7543 / 0.315                                 | 26.36 / 0.7528 / 0.308                                 |
| Ours               | SelfDZSR- $\ell_1$             | 3.2            | <b>27.90 / 0.8164 / 0.337</b>                          | <b>27.67 / 0.8001 / 0.361</b>                          |
|                    | SelfDZSR                       | 3.2            | 27.41 / 0.7836 / <b>0.250</b>                          | 27.21 / 0.7674 / <b>0.265</b>                          |

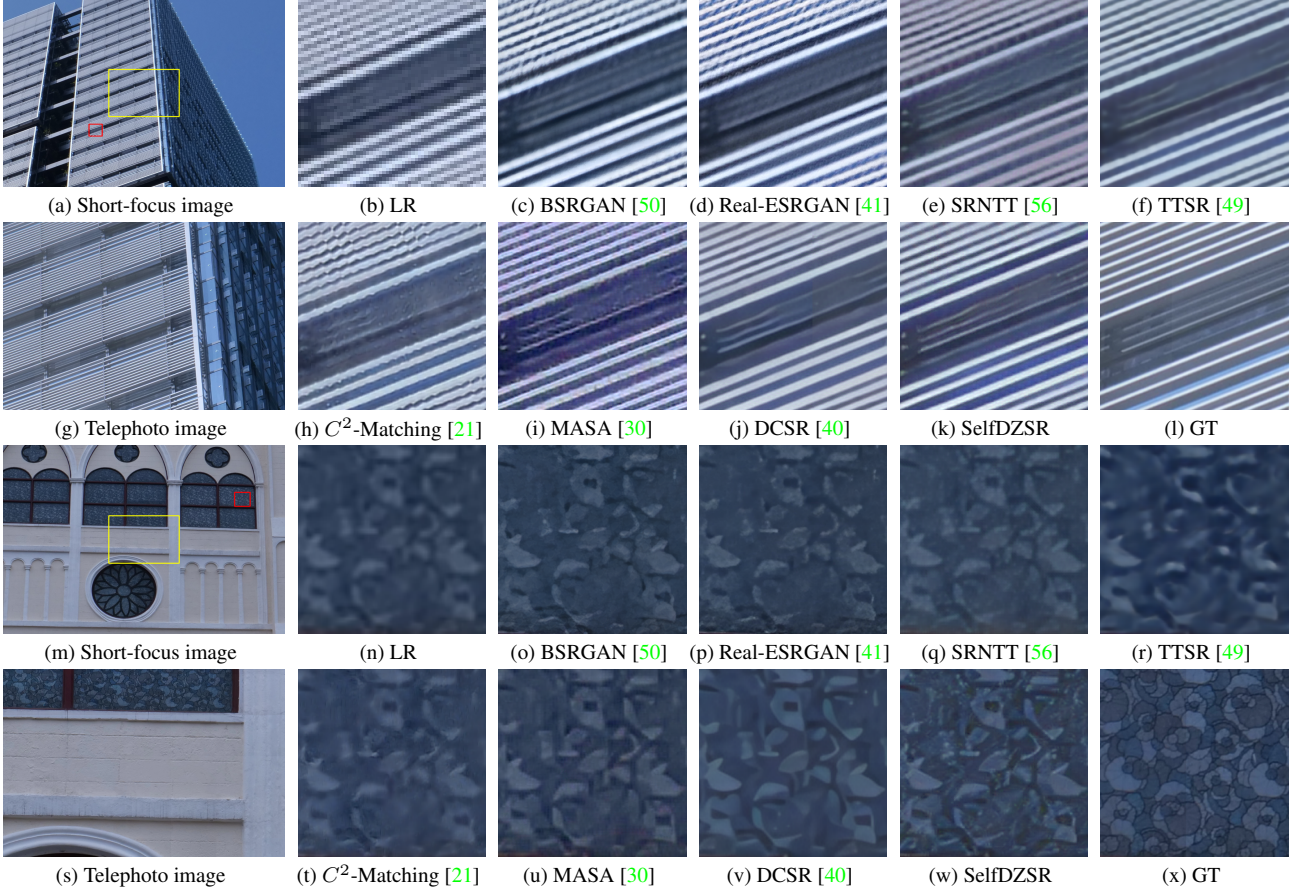


Figure D. Visual comparison on **Panasonic** camera. In the short-focus image, the yellow box indicates the overlapped scene with the telephoto image, while the red box represents the selected LR patch. Our results in sub-figure (k) and (w) restore much more fine details.

Table E. Quantitative results on **Sony** camera with 17 images. We mark the best results **in bold**. The models trained only with  $\ell_1$  (or  $\ell_2$ ) loss are marked in gray. RefSR<sup>†</sup> represents that the RefSR methods are trained in our self-supervised learning manner.

|                    | Method                         | # Param<br>(M) | <i>Full-Image</i>                                      | <i>Corner-Image</i>                                    |
|--------------------|--------------------------------|----------------|--|--|
|                    |                                |                | PSNR $\uparrow$ / SSIM $\uparrow$ / LPIPS $\downarrow$ | PSNR $\uparrow$ / SSIM $\uparrow$ / LPIPS $\downarrow$ |
| SISR               | EDSR [28]                      | 43.1           | 27.12 / 0.8173 / 0.337                                 | 27.13 / 0.8195 / 0.331                                 |
|                    | RCAN [54]                      | 15.6           | 27.42 / 0.8248 / 0.333                                 | 27.40 / 0.8274 / 0.326                                 |
|                    | CDC [44]                       | 39.9           | 27.27 / 0.8207 / 0.357                                 | 27.27 / 0.8228 / 0.351                                 |
|                    | BSRGAN [50]                    | 16.7           | 26.58 / 0.7732 / 0.284                                 | 26.57 / 0.7775 / 0.279                                 |
|                    | Real-ESRGAN [41]               | 16.7           | 26.20 / 0.7816 / 0.262                                 | 26.18 / 0.7876 / 0.256                                 |
| RefSR <sup>†</sup> | SRNTT- $\ell_2$ [56]           | 5.5            | 26.20 / 0.8103 / 0.337                                 | 26.18 / 0.8138 / 0.331                                 |
|                    | SRNTT [56]                     | 5.5            | 26.24 / 0.7969 / 0.290                                 | 26.23 / 0.8001 / 0.283                                 |
|                    | TTSR- $\ell_1$ [49]            | 7.3            | 25.86 / 0.8152 / 0.333                                 | 25.82 / 0.8195 / 0.327                                 |
|                    | TTSR [49]                      | 7.3            | 24.91 / 0.7326 / 0.315                                 | 24.86 / 0.7353 / 0.310                                 |
|                    | $C^2$ -Matching- $\ell_1$ [21] | 8.9            | 26.78 / 0.8221 / 0.327                                 | 26.73 / 0.8254 / 0.322                                 |
|                    | $C^2$ -Matching [21]           | 8.9            | 26.49 / 0.7813 / 0.298                                 | 26.44 / 0.7848 / 0.289                                 |
|                    | MASA- $\ell_1$ [30]            | 4.0            | 27.06 / 0.8149 / 0.306                                 | 27.06 / 0.8189 / 0.301                                 |
|                    | MASA [30]                      | 4.0            | 25.85 / 0.7075 / 0.325                                 | 25.84 / 0.7106 / 0.318                                 |
|                    | DCSR- $\ell_1$ [40]            | 3.2            | 28.49 / 0.8216 / 0.335                                 | <b>28.45</b> / 0.8237 / 0.330                          |
|                    | DCSR [40]                      | 3.2            | 28.08 / 0.8128 / 0.272                                 | 28.03 / 0.8147 / 0.269                                 |
| Ours               | SelfDZSR- $\ell_1$             | 3.2            | <b>28.22</b> / <b>0.8311</b> / 0.292                   | 28.34 / <b>0.8359</b> / 0.303                          |
|                    | SelfDZSR                       | 3.2            | 27.41 / 0.7921 / <b>0.246</b>                          | 27.47 / 0.7948 / <b>0.252</b>                          |

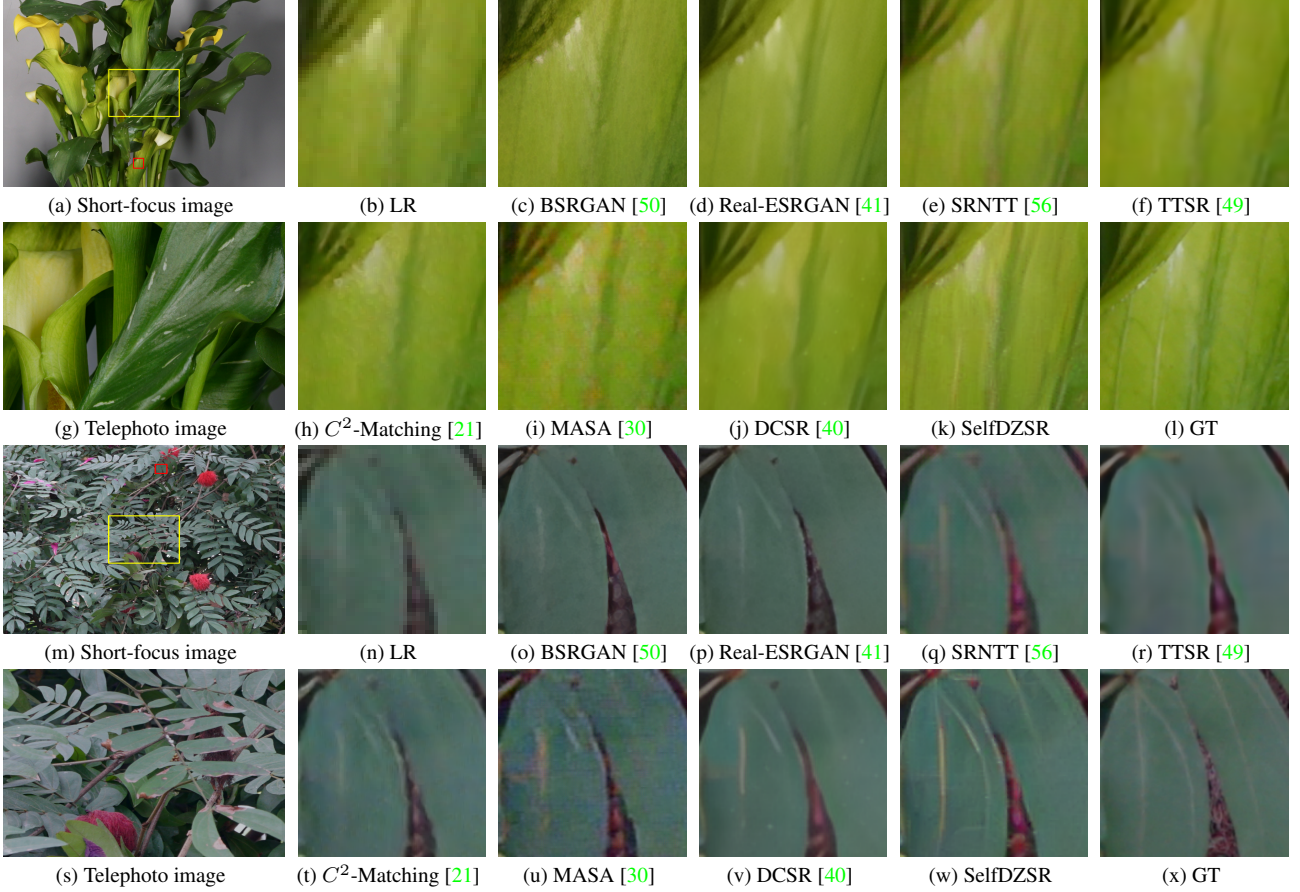


Figure E. Visual comparison on **Sony** camera. In the short-focus image, the yellow box indicates the overlapped scene with the telephoto image, while the red box represents the selected LR patch. Our results in sub-figure (k) and (w) restore much more fine-scale edges.



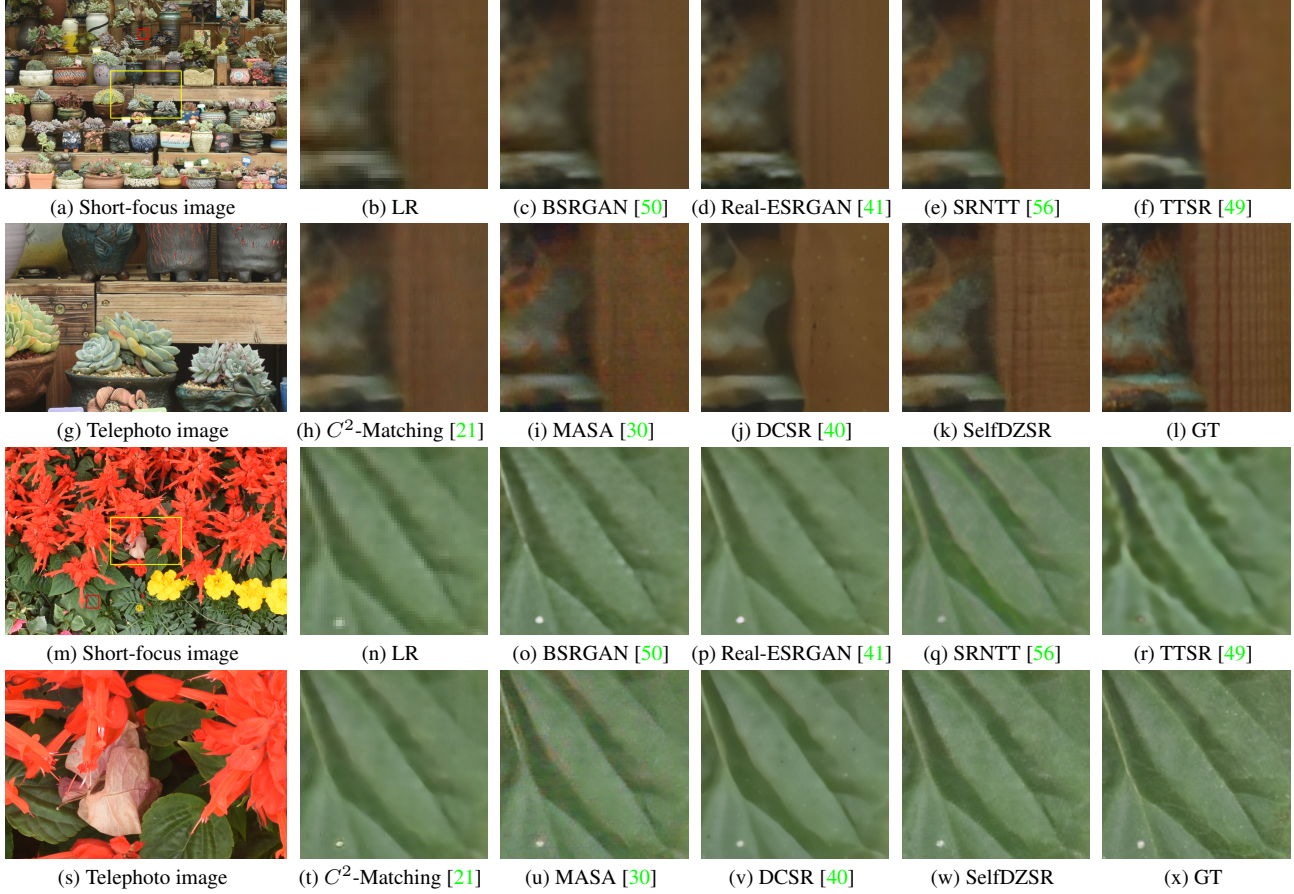


Figure F. Visual comparison on **Nikon** camera. In the short-focus image, the yellow box indicates the overlapped scene with the telephoto image, while the red box represents the selected LR patch. Our result in sub-figure (k) restores much more details, and that in sub-figure (w) is more photo-realistic.

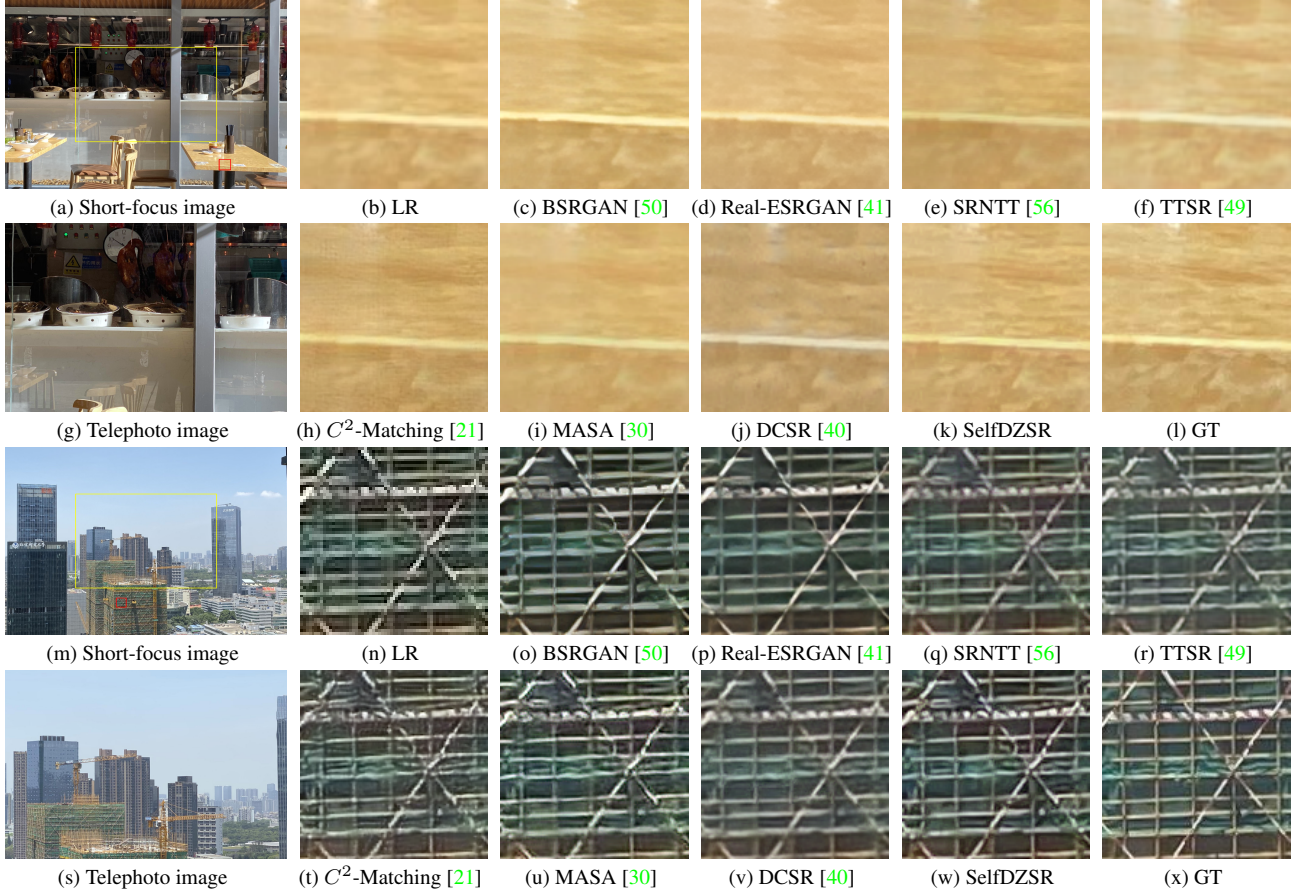


Figure G. Visual comparison on **CameraFusion** dataset. In the short-focus image, the yellow box indicates the overlapped scene with the telephoto image, while the red box represents the selected LR patch. Our result in sub-figure (k) restores much more textures, and that in sub-figure (w) is clearer and more photo-realistic.